Development of a Photometric Stereo Measurement System

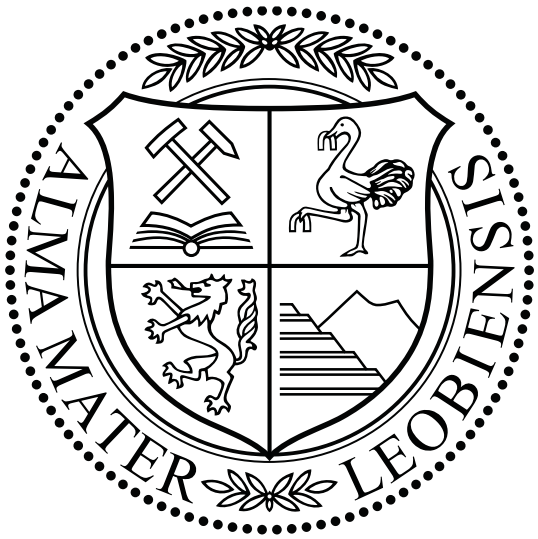

Diploma Thesis

Georg Jaindl

Supervisor
O.Univ.-Prof. Dipl.-Ing. Dr.techn. Paul O'Leary

University of Leoben
Institute for Automation

October 2009

Eidesstattliche Erklärung

Ich erkläre an Eides statt, dass ich diese Arbeit selbstständig verfasst, andere als die angegebenen Quellen und Hilfsmittel nicht benutzt und mich auch sonst keiner unerlaubten Hilfsmittel bedient habe.

Affidavit

I declare in lieu of oath, that I wrote this thesis and performed the associated research myself, using only literature cited in this volume.

Datum / Date	Unterschrift / Signature

Acknowledgment

This thesis, as well as my education, could not have been possible without the help of many people. I would like to thank everyone who helped me throughout the progress of this paper:

Paul O'Leary, my supervisor, for all his time and effort spent on discussions, corrections and inputs;

Gerhard Rath and Gerold Probst for their ideas and support for building the experiment setup;

Matthew Harker for his help with the mathematical background for Photometric Stereo;

Amir Badshah for his help with performing measurements;

Doris Widek, the secretary of the Institute for Automation, for encouragement and necessary coffee breaks;

my Mom and Dad for their lifetime of support and endless love;

my brother, Erich, and sister, Eva, for their guidance throughout our childhood;

my fiancée, Kathryn Kazior, for helping me with my English, in addition to countless back massages, encouragement, and her continuous belief in me;

Cynthia Kazior for her constant supply of M&Ms;

Thomas Kazior for his technical input and his motivation;

my relatives, especially my godmother Heidi and her husband Helmut Tropper;

Maria Zefferer for her supply with pastries and cookies; and

all my friends in Leoben and around the world for making my experience at university unforgettable.

Abstract

Photometric Stereo is an imaging and image processing technique for contact-free surface measurement. It uses the characteristic surface reflectance of materials under different lighting conditions to separate surface albedo from surface geometry. The surface of a stationary test specimen is successively illuminated by light sources with known positions relative to the test specimen and camera. The varying light intensity of each surface element gives information about its orientation. This information about the surface gradient is used to reconstruct a discrete 3D-representation of the surface, i.e. surface reconstruction from gradient fields.

This work describes a fully automated experiment setup for evaluating Photometric Stereo for both ideal and non-ideal Lambertian surfaces. Error sources in the experiment setup were identified and a new calibration method was developed. This method compensates for the inhomogeneous illumination generated by the light sources. For this purpose, the light distribution of each light source was measured and a calibration matrix was derived. The calibration matrix was used to normalize the source data for Photometric Stereo. The error caused by the inhomogeneous light distribution increases with the size of the surveyed specimen. The developed calibration method allows the application of Photometric Stereo on large specimens. It is shown that a square metallic surface with an edge length of 17.5 cm was reconstructed successfully.

Zusammenfassung

Photometric Stereo ist ein Bildgebungs- und verarbeitungsverfahren zur kontaktlosen und nichtzerstörenden Oberflächenvermessung. Dabei wird das charakteristische Reflexionsverhalten eines Probekörpers unter verschiedenen Lichteinfallsrichtungen vermessen um dessen Oberflächenstruktur zu bestimmen. Der stationäre Probekörper wird sukzessive von Lichtquellen mit bekannter Position gegenüber einer Kamera und dem Probekörper beleuchtet. Über die von der Kamera gemessene variierende Lichtintensität jedes Elementes der Oberfläche wird der Oberflächengradient berechnet. Diese Information wird verwendet um ein diskretes 3D-Modell der Oberfläche des Probekörpers zu rekonstruieren, d.h. Oberflächenrekonstruktion aus einem Gradientenfeld.

Diese Arbeit beschreibt einen vollautomatisierten Testaufbau für Photometric Stereo. Dieser wird verwendet um Photometric Stereo für das Vermessen von sowohl idealen als auch nicht idealen Lambertschen Oberflächen zu evaluieren. Die Fehlerquellen im Aufbau wurden identifiziert und eine neue Kalibrierungsmethode entwickelt, welche eine inhomogene Ausleuchtung des Probekörpers durch die Lichtquellen kompensiert. Dafür wurde die Lichtverteilung jeder Lichtquelle vermessen und eine Kalibriermatrix abgeleitet. Mithilfe der Kalibriermatrix werden die Quelldaten für Photometric Stereo normalisiert. Der von der Inhomogenität der Beleuchtung verursachte Fehler wächst mit der Größe des Testkörpers. Die neue Kalibrierungsmethode erlaubt es Photometric Stereo auf große Oberflächen anzuwenden. Es wird gezeigt, dass eine quadratische, metallische Oberfläche mit einer Kantenlänge von 17,5 cm rekonstruiert werden konnte.

Contents

1. Introduction

Photometric Stereo is an imaging and image processing technique for contact-free surface measurement. It was first introduced by Robert J. Woodham in 1979 (see [11]). This method uses the characteristic reflectance of surfaces when illuminated from different directions to separate surface albedo from surface geometry. The surface of a stationary test specimen is successively illuminated by light sources with known positions relative to the test specimen and a camera. The varying light intensity of each surface element gives information about its orientation. This information about the surface gradient is used to reconstruct a discrete 3D-representation of the surface. As opposed to other surface surveying methods, Photometric Stereo offers the following advantages:

1. the experiment setup is static, neither the specimen nor any parts of the experiment setup move; and
2. the measurement is contact-free and non-destructive.

However, as of today, Photometric Stereo is not widely used in machine vision because the necessary consistency and stability of the method for industrial applications has not yet been reached. The following factors limit the use of Photometric Stereo in production environments:

1. the method measures the absolute intensity of the light reflected by the surface; therefore, the measurements need to be performed with high accuracy;
2. the measurements are highly influenced by ambient light, and thus limiting industrial applications;
3. the reflectance behavior of the measured specimen needs to be well known;
4. the algorithm to reconstruct the surface from the measured gradient field is computationally expensive; and
5. the surface structure is not measured absolutely.

1.1. New Approach

In this work, an experimental setup for Photometric Stereo is presented and a new method for calibrating the setup is developed. The method increases the accuracy of the system by partially removing a systematic error caused by the inhomogeneous illumination emitted by

the light sources. The calibration of the setup allows for the measurement of large specimens. It is shown that a square metallic surface with an edge length of 17.5 cm can be successfully reconstructed. Furthermore, the application of Photometric Stereo on non-ideal Lambertian surfaces is evaluated. A diffuse metallic surface, partially covered with oxide scale, is measured and the reconstructed surface analyzed.

2. Reflectance of Surfaces

To derive the method of Photometric Stereo, the reflectance behavior of surfaces needs to be discussed. This chapter gives a short introduction about reflectance modes and describes the Lambertian Reflectance Model, on which the method of Photometric Stereo is based.

2.1. Reflectance Modes

As a light ray impinges upon a surface, it is absorbed, reflected or transmitted. The amount of light reflected in a given direction depends on the optical properties of the surface and the direction of the incident light ray. The most important properties are the microstructure, the spatial and spectral distribution and the state of polarization of the incident illumination [11].

For a flat surface with homogeneous underlying material, the reflected light ray will make an equal angle with the surface normal as the incident ray. Both rays and the surface normal form a plane. This kind of reflection is called specular, metallic or dielectric reflection (see Fig. 2.1a).

Surfaces showing roughness on a microscopic scale scatter an incident light ray into various directions. If the deviation from an ideal plane surface is small, most emergent rays will lie close to the ideal specular direction and the surface will appear glossy (see Fig. 2.1b).

In an inhomogeneous surface layer, light rays are reflected and refracted within the surface numerous times and emerge from the surface near the entry point in a random direction. These surfaces show a diffuse reflectance characteristic (see Fig. 2.1c) [2].

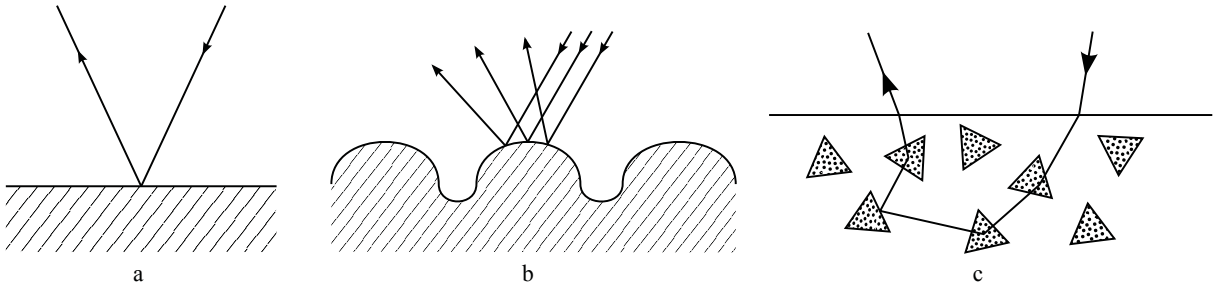

Figure 2.1.: Reflectance modes according to [2]: a) specular reflection; b) glossy reflection; c) diffuse reflection.

2.2. Reflectance Models

Most materials show a combination of these reflectance modes. A reflectance model characterizes the optical properties of a specific surface material and predicts the reflected light intensity received by an observer. For this purpose, the orientation of the light source and the observer relative to the surface is defined as follow (see Fig. 2.2):

1. i is the angle between the surface normal and the vector pointing at the light source;
2. e is the angle between the surface normal and the vector pointing at the observer; and
3. g is the phase angle between the vector pointing at the light source and the vector pointing at the observer;

so that the direction of the incident light ray, the emergent light ray and the plane formed by the two rays is well defined [11].

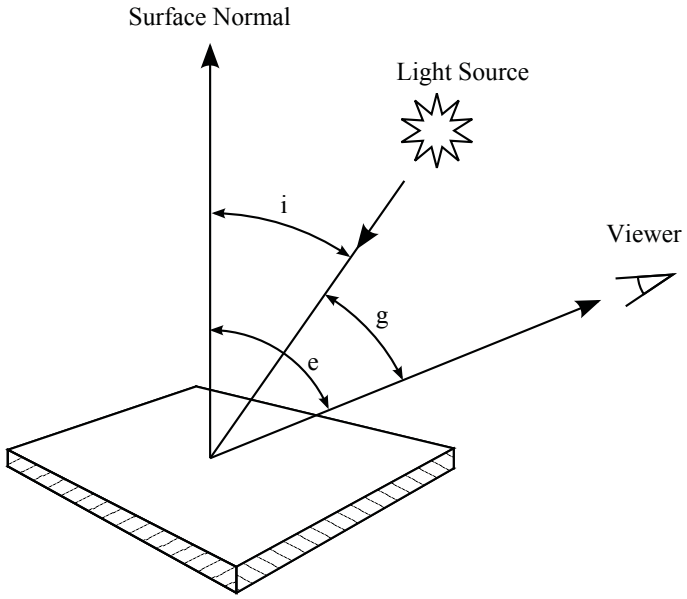

Figure 2.2.: Definition of the relative position between surface, light source and observer: i is the angle between the surface normal and incident light ray; e is the angle between the surface normal and emergent light ray in the direction of the observer; and g is the angle between the incident and emergent light ray (according to [11]).

2.3. The Lambertian Reflectance Model

If the incident angle i is greater than zero, a surface patch will appear foreshortened as seen from the position of the lightsource. Given a collimated incident illumination, the luminous flux $\mathrm{d}\Phi$ passing through the area $\mathrm{d}A_s$ impinges upon a surface patch with the area $\mathrm{d}A$. The

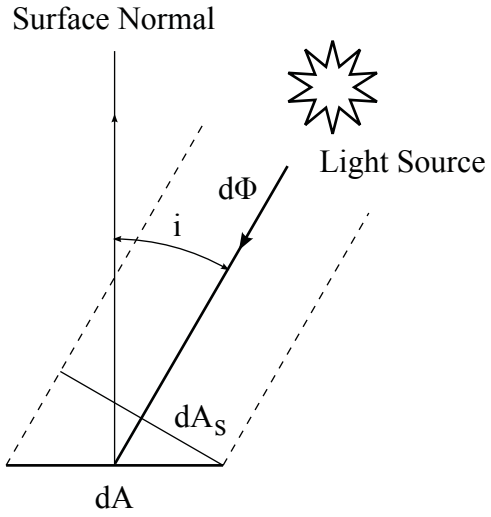

Figure 2.3.: Irradiance upon a tilted surface patch: the incident flux $\mathrm{d}\Phi$ is distributed over a surface element $\mathrm{d}A$. $\mathrm{d}A_s$ is the foreshortened surface patch as seen from the position of the light source.

proportionality factor between the areas $\mathrm{d}A$ and $\mathrm{d}A_s$ is the cosine of the incident angle (see Fig. 2.3).

$$\mathrm{d}A_s = \cos(i)\ \mathrm{d}A\ . \tag{2.1}$$

For a constant incident luminous intensity $I = \frac{\mathrm{d}\Phi}{\mathrm{d}A_s}$, the irradiance $E = \frac{\mathrm{d}\Phi}{\mathrm{d}A}$ on the surface decreases as i increases,

$$E = \frac{\mathrm{d}\Phi}{\mathrm{d}A} = \cos(i)\frac{\mathrm{d}\Phi}{\mathrm{d}A_s} = \cos(i)\ I\ . \tag{2.2}$$

This means that the luminous flux $\mathrm{d}\Phi$ received by a surface patch decreases when the light source and the surface form a smaller angle.

The surface patch $\mathrm{d}A$ appears foreshortened to a spectator as the emergent angle e increases. Assuming the use of a camera with orthographic imaging and a pixel size $\mathrm{d}A_p$, the surface area $\mathrm{d}A_o$ observed by one pixel increases by the same amount as $\mathrm{d}A$ is foreshortened,

$$\mathrm{d}A_o = \frac{\mathrm{d}A_p}{\cos(e)}\ . \tag{2.3}$$

This means that the flux Φ received by a camera pixel remains constant when the emergent angle e changes (see Fig. 2.4),

$$\Phi \sim \cos(e)\ \mathrm{d}A_o = \mathrm{d}A_p\ . \tag{2.4}$$

In other words, an idealized diffuse (Lambertian) surface appears to an observer equally bright in all viewing directions. However, the light intensity received by the observer depends on the direction of the incident illumination on the specimen. The observed light intensity decreases

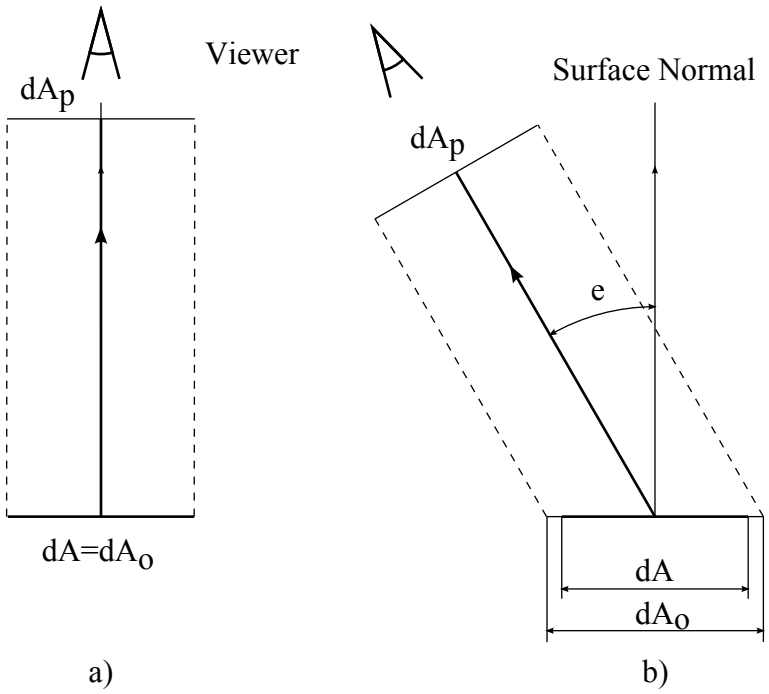

Figure 2.4.: Light irradiance on a camera pixel: a) a camera with orthographic projection and a pixel size $\mathrm{d}A_p$ observes a surface patch of the same size $\mathrm{d}A_o = \mathrm{d}A_p$; b) if the viewing direction of the camera is changed, the area observed by the pixel increases with the reciprocal cosine of the angle e: $\mathrm{d}A_o = \mathrm{d}A_p / \cos(e)$.

as the incident light forms a smaller angle with the surface [2]. The reflectance function for this surface can now be written as

$$\phi(i, e, g) = \rho \ \cos(i) \ , \tag{2.5}$$

where ρ is a reflectance factor and i is the angle between the surface normal and the incident light. The reflectance factor ρ depends on the intensity of the incident illumination and the distance between the observer and the surface. For non-ideal Lambertian surfaces, ρ also depends on the fraction of reflected versus absorbed light. This is a simplified form of Lambert's cosine law [11]. The derivation of the method of Photometric Stereo using this model is shown in Section 3.

2.4. The Bidirectional Reflectance Distribution Function

When the position of the light source and the observer is known, a reflectance map shows the reflected light intensity of a surface as a function of the surface normal vector in a Cartesian coordinate system.

A surface patch described by the function $z = f(x, y)$, has the surface normal vector,

$$\boldsymbol{n} := \left[-\frac{\partial f(x,y)}{\partial x}, -\frac{\partial f(x,y)}{\partial y}, 1 \right]^{\mathrm{T}} \ . \tag{2.6}$$

Defining the parameters p and q as

$$p := \frac{\partial f(x,y)}{\partial x} \ \ and \ \ q := \frac{\partial f(x,y)}{\partial y} \ , \tag{2.7}$$

the surface normal vector can be written as

$$\boldsymbol{n} = [-p, -q, 1]^{\mathrm{T}} \ . \tag{2.8}$$

Assuming the viewer is positioned at the z-axis above the surface, the vector pointing at the viewer can be defined as

$$\boldsymbol{v} := [0, 0, 1]^{\mathrm{T}} \ , \tag{2.9}$$

and the vector pointing at the light source as

$$\boldsymbol{s} := [p_s, q_s, 1]^{\mathrm{T}} \tag{2.10}$$

(see Fig. 2.5).

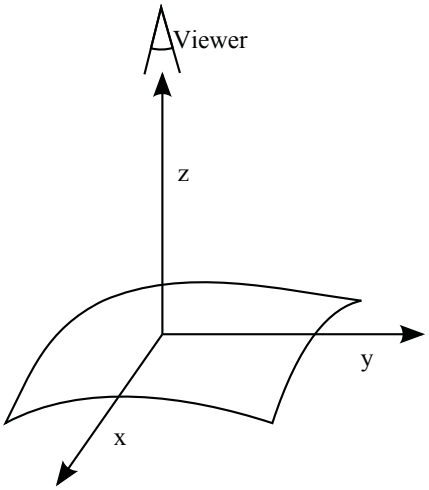

Figure 2.5.: Viewer oriented coordinate system, i.e. viewer looking in direction $[0, 0, -1]^{\mathrm{T}}$.

Now the cosines of the incident, emergent and phase angle can be calculated using normalized dot products:

$$\cos(i) = \frac{\boldsymbol{n} \cdot \boldsymbol{s}}{|\boldsymbol{n}| \cdot |\boldsymbol{s}|} = \frac{1 - p \cdot p_s - q \cdot q_s}{\sqrt{1 + p^2 + q^2} \cdot \sqrt{1 + p_s^2 + q_s^2}} \; ; \tag{2.11}$$

$$\cos(e) = \frac{\boldsymbol{n} \cdot \boldsymbol{v}}{|\boldsymbol{n}| \cdot |\boldsymbol{v}|} = \frac{1}{\sqrt{1 + p^2 + q^2}} \; ; and \tag{2.12}$$

$$\cos(g) = \frac{\boldsymbol{s} \cdot \boldsymbol{v}}{|\boldsymbol{s}| \cdot |\boldsymbol{v}|} = \frac{1}{\sqrt{1 + p_s^2 + q_s^2}} \; . \tag{2.13}$$

For a given position of the light source, these relationships can be used to transform a reflectance function $\phi(i, e, g)$ into a bidirectional reflectance distribution function (BRDF) $R(p, q)$. This function will show the reflected light intensity seen by an observer as function of the surface orientation [11].

For a Lambertian surface with the reflectance function $\phi(i, e, g) = \rho \, \cos(i)$, the BRDF has the form

$$R(p, q) = \rho \, \frac{1 - p \cdot p_s - q \cdot q_s}{\sqrt{1 + p^2 + q^2} \cdot \sqrt{1 + p_s^2 + q_s^2}} \; . \tag{2.14}$$

The reflectance map of this BRDF for the given position of the light source with $\boldsymbol{s} = [0.7, 0.3, 1]^{\mathrm{T}}$ is shown in Figure 2.6.

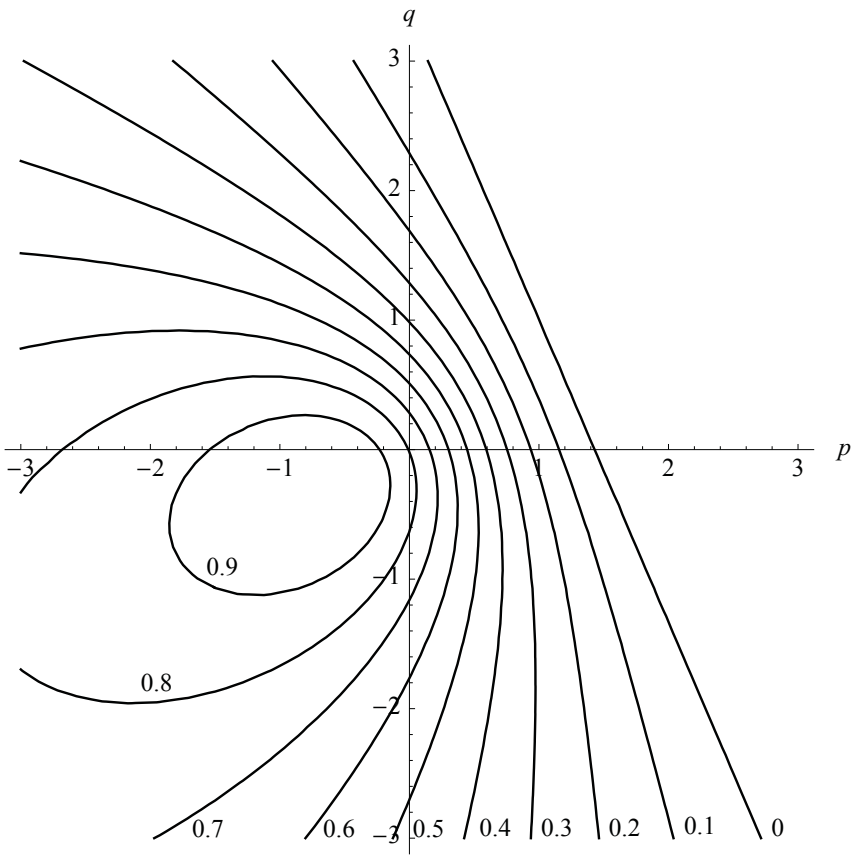

Figure 2.6.: Reflectance map for a Lambertian Surface with $\rho = 1$ and position of the light source given by $p_s = 0.7$ and $q_s = 0.3$.

3. Photometric Stereo

Photometric Stereo is a method to separate surface albedo from surface structure. The idea of Photometric Stereo is to vary the direction of incident illumination on a surface, while holding the viewing direction and the position of the surveyed surface constant [11]. For a known reflectance behavior of the object material, the orientation of a surface patch, and therefore its normal vector $\boldsymbol{n}$, can be determined by inverting the BRDF described in Section 2.4. In the following section, the method of Photometric Stereo is derived for the Lambertian Reflectance Model according to [11].

3.1. Calculating the Surface Gradient

A Lambertian surface is characterized by the reflectance function in Equation 2.14. Presuming $\boldsymbol{n}$ and $\boldsymbol{s}$ are unit vectors, this function is linear in terms of p, q , and ρ. Generally, the orientation of the surface and the reflectance factor ρ is unknown, so that the reflected light intensity I for three different illumination directions needs to be measured to solve the BRDF. For a given surface patch (x, y), the following linear equation system can be formed:

$$I_1 = R_1(p, q) \; ; \tag{3.1}$$

$$I_2 = R_2(p, q) \; ; \; and \tag{3.2}$$

$$I_3 = R_3(p, q) \; . \tag{3.3}$$

This equation system can be formulated as a matrix equation. For this reason, let

$$\tilde{\boldsymbol{I}} := [I_1, I_2, I_3]^{\mathrm{T}} \tag{3.4}$$

be the column vector of intensity values recorded at (x, y) in each of the three views. Further, let

$$\tilde{\boldsymbol{s}}_1 := [s_{11}, s_{12}, s_{13}]^{\mathrm{T}} \; ; \tag{3.5}$$

$$\tilde{\boldsymbol{s}}_2 := [s_{21}, s_{22}, s_{23}]^{\mathrm{T}} \; ; \; and \tag{3.6}$$

$$\tilde{\boldsymbol{s}}_3 := [s_{31}, s_{32}, s_{33}]^{\mathrm{T}} \; ; \tag{3.7}$$

be unit column vectors defining the direction from the surface patch (x, y) to the light sources. The matrix $\tilde{N}$ is then formed as

$$\tilde{\mathsf{N}} := \begin{bmatrix} \tilde{\boldsymbol{s}}_1{}^{\mathrm{T}} \\ \tilde{\boldsymbol{s}}_2{}^{\mathrm{T}} \\ \tilde{\boldsymbol{s}}_3{}^{\mathrm{T}} \end{bmatrix} = \begin{bmatrix} s_{11} & s_{12} & s_{13} \\ s_{21} & s_{22} & s_{23} \\ s_{31} & s_{32} & s_{33} \end{bmatrix} \; . \tag{3.8}$$

Let

$$\tilde{\boldsymbol{n}} := [n_1, n_2, n_3]^{\mathrm{T}} \tag{3.9}$$

be the column unit vector normal to the surface at (x,y), then

$$\tilde{\boldsymbol{I}} = \rho \tilde{\mathsf{N}} \tilde{\boldsymbol{n}} \tag{3.10}$$

and

$$\rho \tilde{\boldsymbol{n}} = \tilde{\mathsf{N}}^{-1} \tilde{\boldsymbol{I}}. \tag{3.11}$$

The surface normal $\tilde{\boldsymbol{n}}$ is a unit vector, so that

$$\rho = \left| \tilde{\mathsf{N}}^{-1} \tilde{\boldsymbol{I}} \right| \tag{3.12}$$

and

$$\tilde{\boldsymbol{n}} = \frac{1}{\rho} \tilde{\mathsf{N}}^{-1} \tilde{\boldsymbol{I}} \, . \tag{3.13}$$

A solution to Equation 3.13 exists only if $\tilde{\mathsf{N}}$ is non-singular. In other words, the vectors $\tilde{\boldsymbol{s}}_1, \tilde{\boldsymbol{s}}_2, \tilde{\boldsymbol{s}}_3$ that form N need to be linearly independent. For the application of Photometric Stereo, this means that the light sources and the observed surface patch must not form a plane.

According to Equation 2.6 the gradient of the surface element can be calculated as

$$p = -\frac{n_1}{n_3} \; and \; q = -\frac{n_2}{n_3} \, . \tag{3.14}$$

The surface normal vector can then be formed as

$$\boldsymbol{n} = \begin{bmatrix} -p \\ -q \\ 1 \end{bmatrix} \, . \tag{3.15}$$

3.2. Reconstructing the Surface

If the light intensity is measured over a grid of surface patches, the discrete gradient field of the surface can be determined. The reconstruction of the surface is done by numeric integration over the gradient field. The mathematical background of the discrete surface reconstruction from a measured gradient field has been discussed by Matthew Harker and Paul O'Leary, who kindly provided a Matlab implementation of their method [1]. The used algorithm reconstructs a discrete surface from a gradient field so that scaling of the calculated height map matches the image coordinates. Figures of surfaces presented in this work use pixel units that can be transformed to metric units as described in Section 4.1.1.

4. Experiment Setup

To evaluate the method of Photometric Stereo, an experiment setup was designed. One major aspect of the setup was to test Photometric Stereo under ideal conditions. To achieve this, the illumination and the image acquisition was optimized (see Section 4.1 and 4.2), and a method of calibrating the test stand was developed (see Section 5.1).

The setup contained the optical arrangement for the illumination and image acquisition (see Fig. 4.4), as well as a control unit (Fig. 4.11) and the software implementation of the image processing.

The experiment setup was enclosed in a light-proof cover to shield ambient light. Standard power supplies for artificial light sources operate with 50 Hz alternating current. Therefore, standard AC light sources emit pulsating light with 100 peaks per second. The camera used for observing the scene acquired images at a frame rate of 30 Hz. In a continuous video stream from the camera, this would lead to a significant beat. Photometric Stereo is based on precise measurement of light intensities, so that pulsating ambient light would lead to an unpredictable error and render the measurement incorrect.

For the experiment setup, four, instead of the minimum of three light sources, were used. The fourth illumination case delivers additional data about the surface structure of the test specimen and reduces the influence of camera noise (see Section 5.2). Additionally, specular behavior of surfaces can be partially compensated by excluding the illumination case where the specular reflection appears. This way of dealing with specularity was discussed by [7] and [8], but is not covered in this work. The light sources were arranged at equal distances d_l from the optical axis of the camera (see Fig. 4.2). Below this optical setup, a specimen stage was installed. The chosen dimensions of the setup are shown in Table 4.1.

The global coordinate system was chosen so that its origin lay on the specimen stage and the z-axis pointed at the focal point of the camera.

4.1. Image Acquisition

A camera projects an image of the observed scene on a CCD grid. The light intensity reflected by a specimen can be measured for multiple positions on its surface simultaneously. Using the method of Photometric Stereo, the surface gradient for each measured surface patch is calculated. This grid of numerical gradients forms the discrete gradient field of the surface.

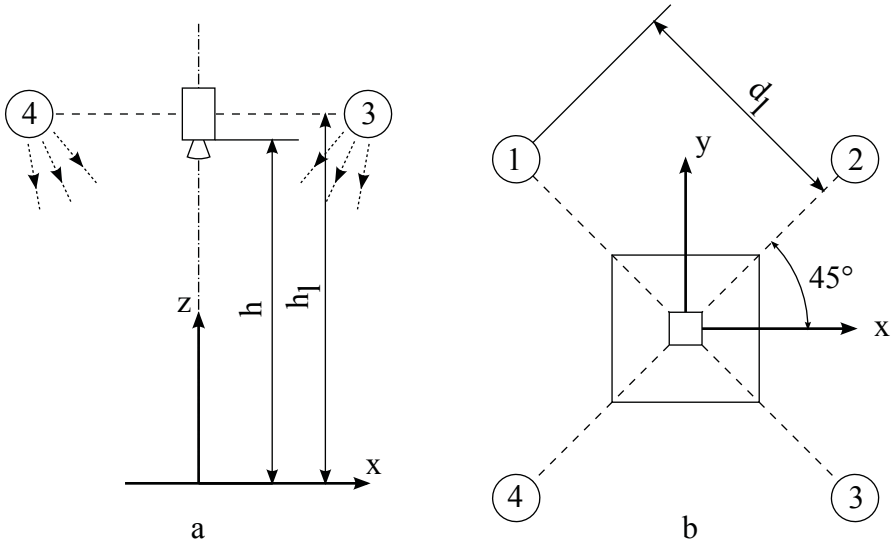

Figure 4.1.: Schematic experiment setup: a) Front view: h: height of camera over origin, h_l: height of lights over origin; b) Top view: d_l: distance of light sources from optical axis.

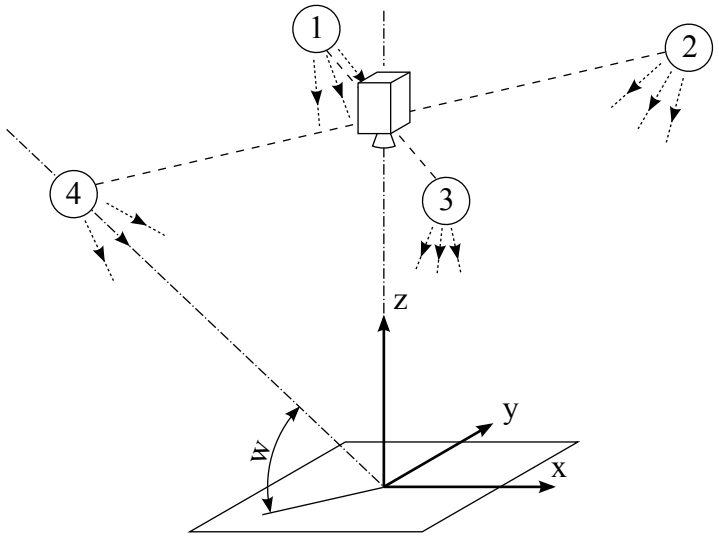

Figure 4.2.: Schematic experiment setup - Isometric view: w: angle between optical axis of light source and specimen stage.

Description	Symbol	Value [mm]
Distance of camera to specimen stage	h	975
Distance of light sources to specimen stage	h_l	920
Distance of light sources to optical axis	d_l	410
Specimen height	h_0	$variable$
Distance of camera to specimen surface	h_c	$h - h_0$
Angle between specimen stage and axis of light sources	w	65°

Table 4.1.: Dimensons of the experiment setup

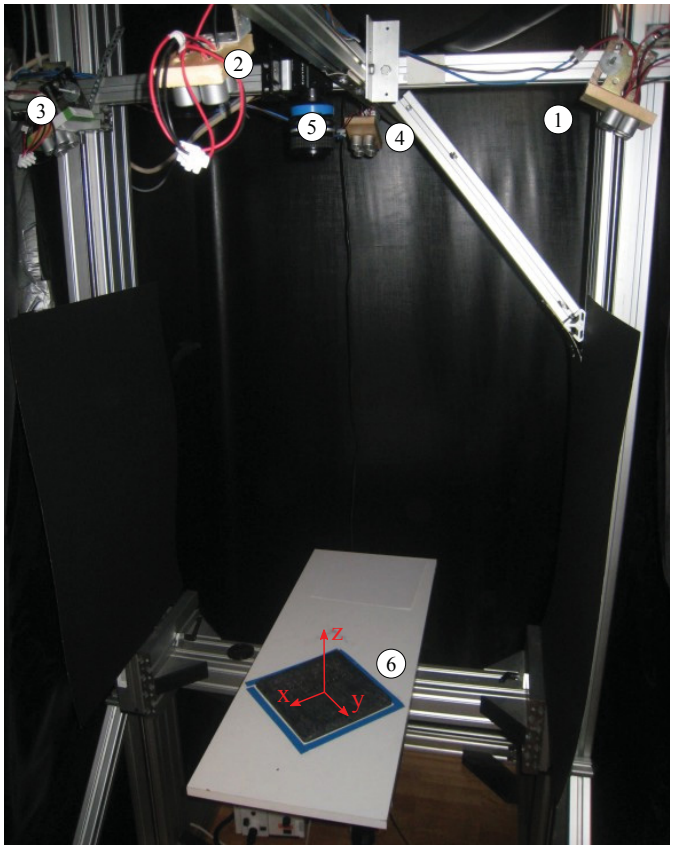

Figure 4.3.: Experiment setup: 1-4) Light Sources; 5) Camera; 6) Test Specimen with overlaid coordinate system.

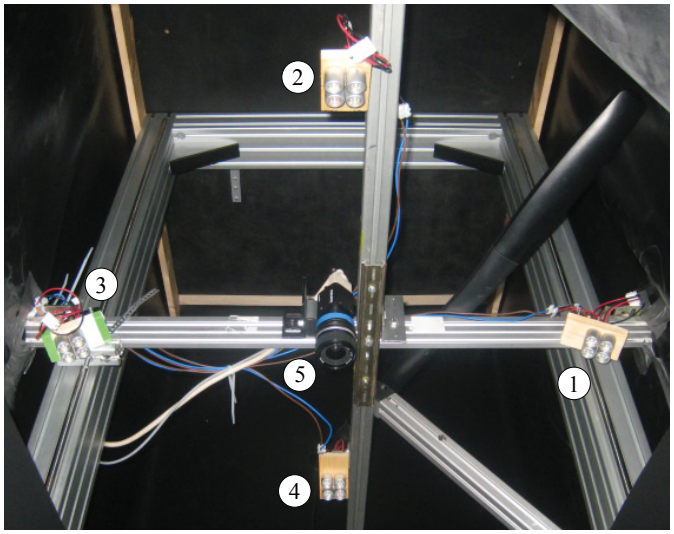

Figure 4.4.: Camera and light setup: 1-4) Light sources; 5) Camera.

A *Pulnix TM-1402CL* camera equipped with a *Nikon Nikkor 24 mm* lens was used for image acquisition. The camera was connected through a Camera Link interface to a *National Instruments PCI-1428* frame grabber. The frame grabber was controlled with *Matlab's Image Acquisition Toolbox*.

4.1.1. Image Coordinates

The maximum resolution of the used camera is 1392x1040 pixels. To survey a square area on the specimen stage, the camera was adjusted to output an image of 1040x1040 pixels. Given the lens zoom and the setup dimensions, the image represents an area of $176\text{x}176\,\text{mm}^2$ on the specimen stage. The pixel resolution can be calculated to be

$$R_x = R_y = \frac{1040\,\text{pixels}}{176\,\text{mm}} = 5.9\,\frac{\text{pixels}}{\text{mm}}\ . \tag{4.1}$$

In computer vision, a pixel is addressed using an image coordinate system (see Fig. 4.5). The transformations between the global coordinate system (x, y, z) defined in Section 4 and the image coordinates $(\hat{x}, \hat{y}, \hat{z})$ are

$$x = -\frac{176}{2} + \frac{176}{1040}\hat{x}\ ; \tag{4.2}$$

$$y = \frac{176}{2} - \frac{176}{1040}\hat{y}\ ;\ and \tag{4.3}$$

$$z = \hat{z}\ . \tag{4.4}$$

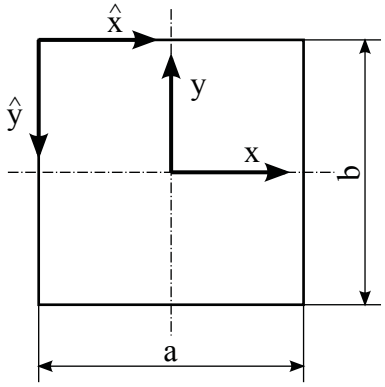

Figure 4.5.: Global coordinate system (x, y) and image coordinate system $(\hat{x}, \hat{y})$. The dimensions of the image area are a=b=176 mm.

4.1.2. Camera Linearity

Unlike other surface surveying methods, Photometric Stereo is based on exact measurement of the reflected light intensity of a surface patch. Therefore, the camera needs to fulfill two basic requirements for measurement devices: linearity with the input signal and a high signal-to-noise ratio (SNR). The *Pulnix TM-1402CL* camera offered a SNR of 52 dB [6]. To further improve the SNR, 100 frames per illumination direction were taken and averaged. The increase of the SNR from this procedure is given by

$$SNR_n = SNR\,\sqrt{n}\,, \tag{4.5}$$

where n is the number of averaged frames. The increase of the SNR for 100 frames is 20 dB so that a total SNR of 72 dB was reached.

The camera is equipped with a 1/2" monochrome progressive scan CCD sensor in conjunction with a 10 bit analog digital converter. Before the signal is transmitted over the *Camera Link* interface, the 10 bit image is downscaled into an 8 bit image using a look-up table (LUT). The LUT can be used to enhance the contrast of images or calibrate the camera for providing an improved linear response.

A CCD sensor integrates the number of impinging photons on a pixel over the exposure time of the CCD. The photo diode of the pixel generates an electric potential that linearly increases with the number of photons received by the pixel. This signal is amplified and converted into a digital value by an analog to digital converter (ADC). For a constant light incidence on a pixel and a given exposure time, a certain quantity of photons will impinge on the pixel. If the exposure time is changed, the number of photons reaching the pixel changes proportionally with the exposure time. The ADC was calibrated by comparing the 8 bit value for a given pixel at the exposure times of 1/30 s and 1/60 s. The LUT was then adjusted so that for each pixel the pixel value at an exposure time of 1/30 s is twice the pixel value at 1/60 s. The diagrams in Figure 4.6 shows the uncalibrated state of the camera; Figure 4.7 shows the response of the camera after the calibration using a LUT; Figure 4.8 shows the LUT that was used for the calibration.

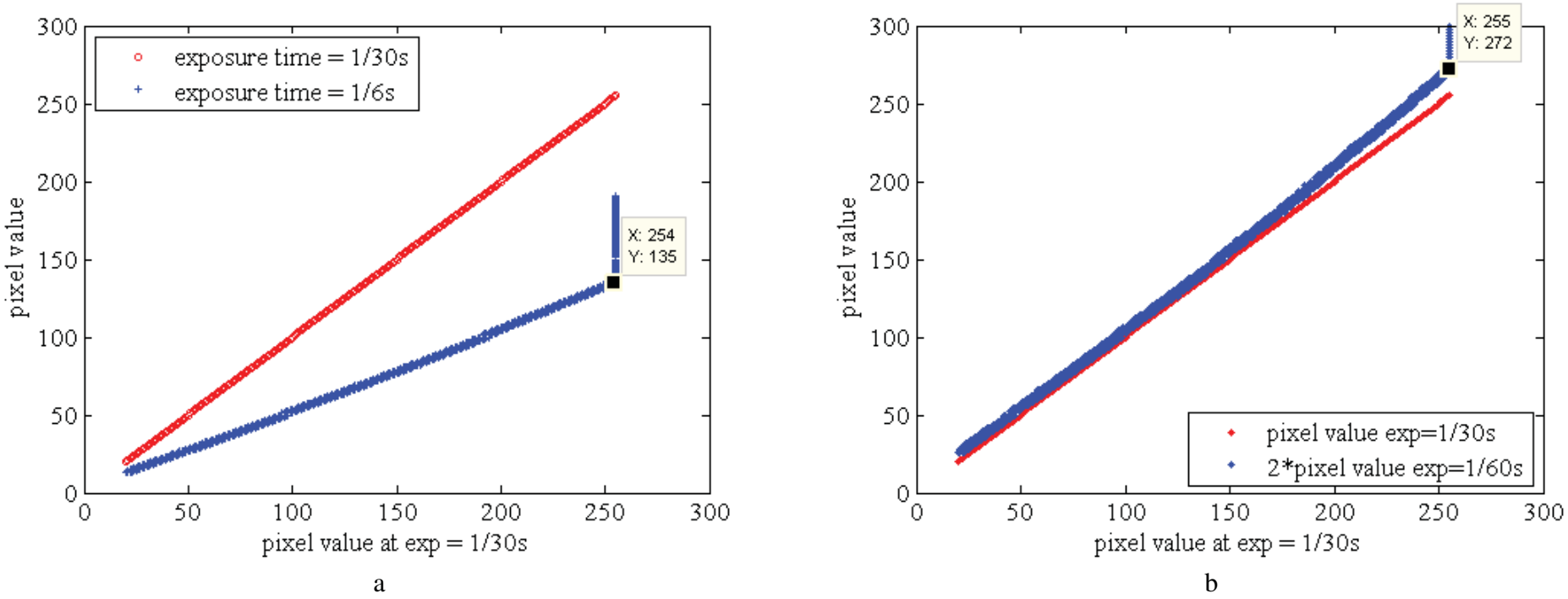

Figure 4.6.: Uncalibrated Pulnix TM-1400CL camera: a) each pixel value at an exposure time of 1/60 s is compared to the corresponding pixel value at an exposure time of 1/30 s. At the marked point, the pixel value at 1/60 s is 135, while the expected value is $254/2 = 127$. This is an aberration of 6.3%; b) for a better visualization of the error, the values at 1/60 s are multiplied by two. In case of an ideal linear camera response, the lines should match. However, for pixel values of 150 and greater, a significant gap between the lines is visible.

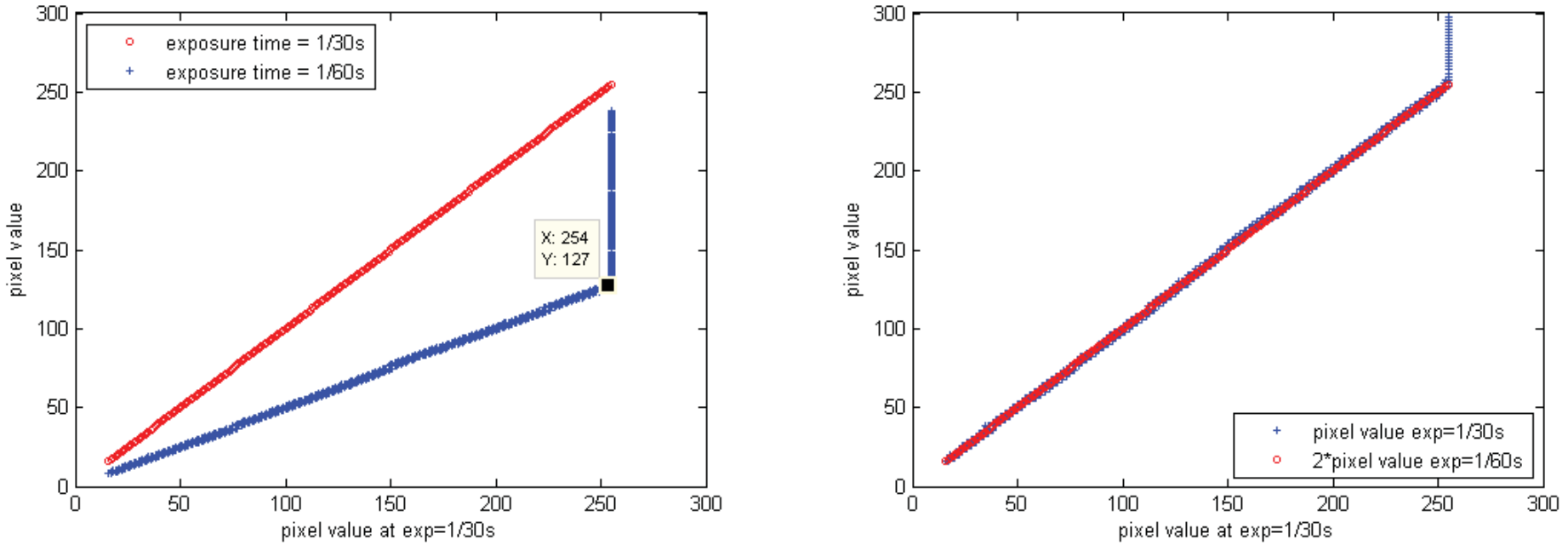

Figure 4.7.: Calibrated Pulnix TM-1400CL camera : a) the pixel value at an exposure time of 1/60 s is two times the pixel value at an exposure time of 1/30 s; b) for a better visualization of the error, the values at 1/60 s are multiplied by two. In case of an ideal linear camera response, the lines should match. As seen in the figure, the aberration between the lines is negligible.

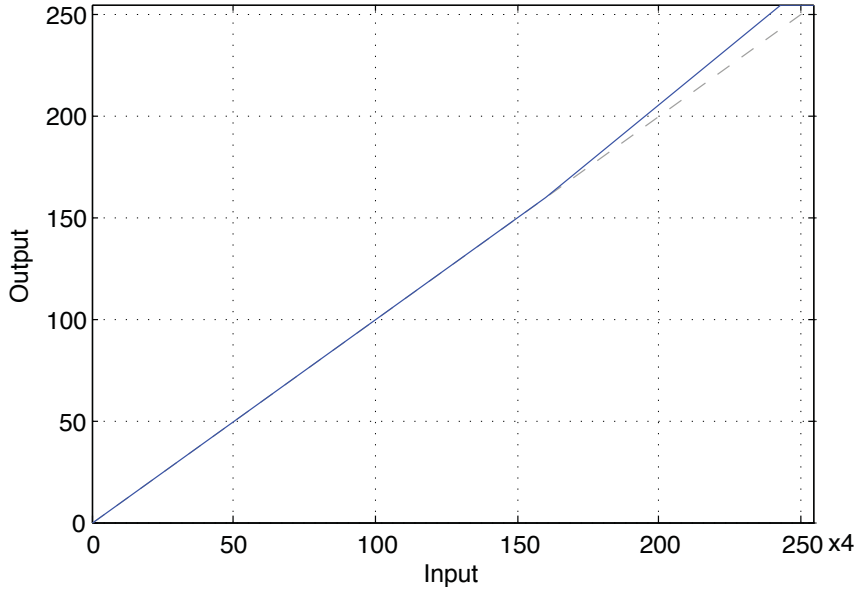

Figure 4.8.: Look Up Table used in the Pulnix TM1400-CL camera for conversion of a 10 bit value into an 8 bit value. The linearity of the camera is calibrated with two knees at $[160, 160]$ and $[243, 255]$.

4.1.3. Exposure Time

The camera exposure time that delivers the best quality image depends on the maximum light intensity received by the CCD. For a high reflecting surface, a short exposure time is used. The smaller the light intensity received by the camera sensor, the longer the CCD needs to be exposed. In order to directly compare the intensity values of pictures taken with different exposure times, all pictures were amplified to a reference exposure time of 1/30 s. Given a linear camera sensor, this conversion is done as follows: let I_e be a picture acquired with an exposure time of e seconds. The referenced Image I_r is then

$$I_r := I_e \frac{1/30}{e} \,. \tag{4.6}$$

All images acquired in this work are scaled to the reference exposure time of 1/30 s. The intensity values of pictures exceeding the camera's dynamic range of 255 are due to this amplification.

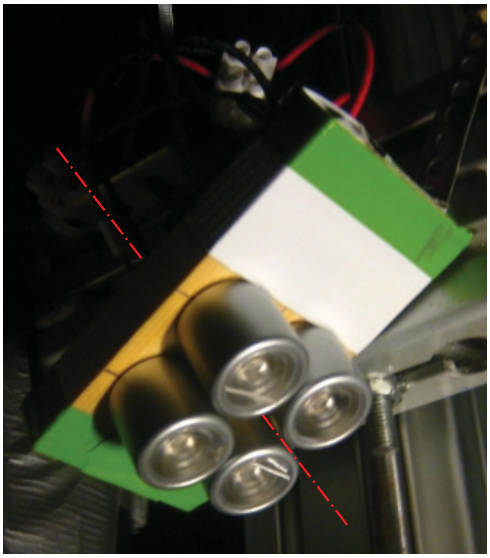

Figure 4.9.: Light block with optical axis.

4.2. Light Sources

Each light source was assembled from four *Osram Dragoneye (DE1-Y2)* LEDs (see Fig. 4.9). This type of LEDs are embedded inside a reflector so that the emitted light can be channeled into a given direction. The use of multiple LEDs per light source increased the light intensity so that the distance between the light source and the specimen could be increased. The increased distance improved the homogeneity of the illumination since the distance is closer to the ideal case of infinity. The LEDs radiate yellow light at a wavelength of 589 nm and each have a power consumption of 0.8 W. For an optimal scene illumination, the adjustment of the light sources is fundamental. The LEDs were adjusted so that their axes coincide with the origin of the global coordinate system. The adjustment was validated with the camera (see Fig. 4.10).

In order to fully automate the experiment setup, the lights were controlled by a *Beckhoff BK9000* bus coupler. This coupler ships with a software bundle including an OPC server. Using Matlab's OPC Toolbox, the system was controlled over a TCP/IP connection. For switching the light sources, four *Schrack MT3210C4* relays were connected to a *KL2134* digital output module of the coupler. The relays were fed by a *Lytron NG-2500* DC power supply with a current limit of 350 mA to prevent the LEDs from being overloaded. An additional *KL3102* analog input module was used to measure the light source voltage. A *Fluke 85III* Multimeter was used to fine-tune the current provided by the power supply (see Fig. 4.11).

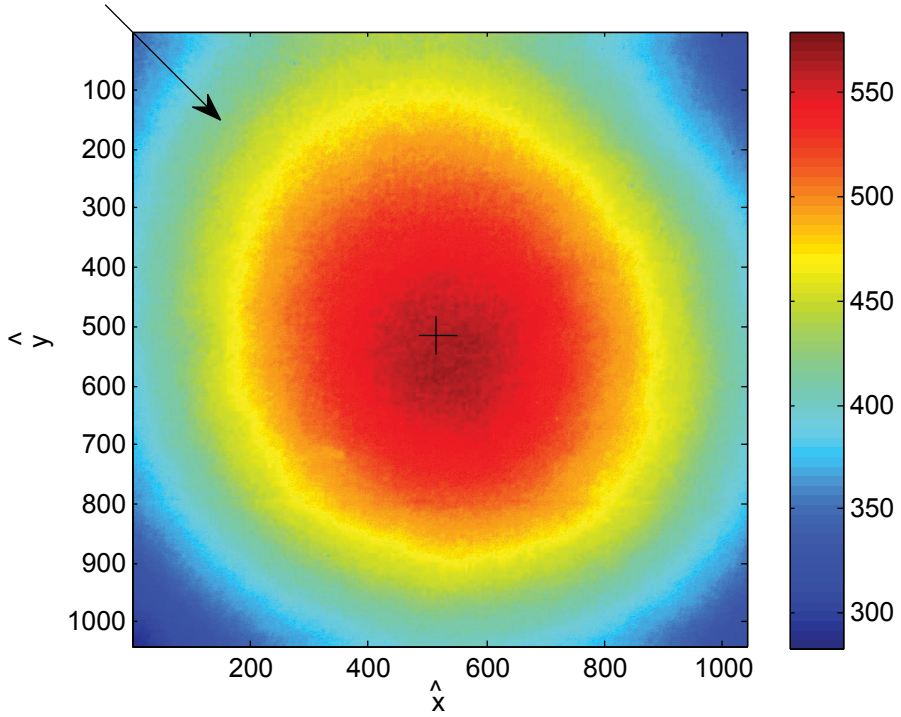

Figure 4.10.: Light distribution of Light Source 1 on a plane white surface as seen by the camera. The arrow depicts the direction of the incident light. The cross shows the origin of the global coordinate system. The light sources were adjusted so that the spot with the highest intensity matches the origin of the global coordinate system.

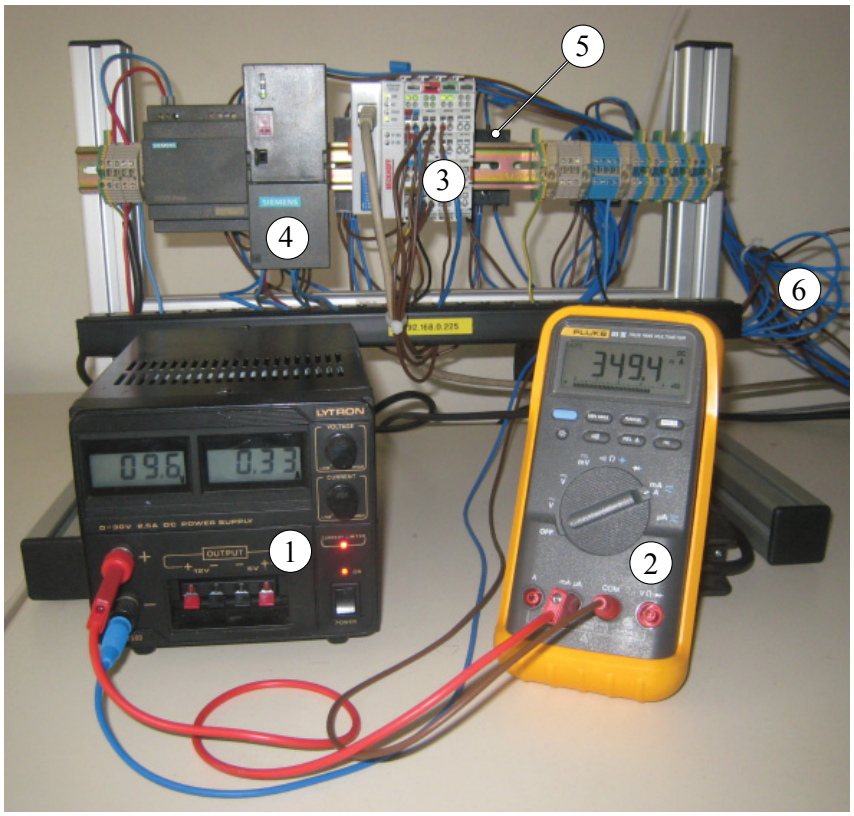

Figure 4.11.: Control unit for the light sources: 1) Power supply for powering the relays; 2) Ammeter; 3) Bus coupler with digital output and analog input module; 4) Power supply for the bus coupler 5) Relays 1-4; 6) Wires to the light sources.

4.2.1. LED Behavior

The method of Photometric Stereo is based on measuring the light intensity reflected by a surface under different illumination directions. In order to compare the reflection factors of different materials, the illumination conditions need to be well known. While the illumination direction is defined by the physical setup, the light intensity of the used light sources can vary. One major factor determining the light intensity radiated by a LED is its temperature. During their operation time, LEDs warm up so that their light intensity decreases.

Figure 4.12 shows the light intensity over the LEDs operation time. Right after the light is switched on, the intensity peaks. After 5 seconds, it slowly falls till it reaches the thermal equilibrium after 50 minutes. The waiting time after the light switches on and before the image acquisition for Photometric Stereo starts was chosen to be 10 seconds. The image acquisition per light source (see Section 4.1) is finished in about 6-7 seconds. In this time window, the light intensity falls by 0.25%. This change is insignificant and can be neglected. However, if multiple measurements are performed in a short time, the light sources get warm and invalidate the calibration of the setup (see Section 5.1).

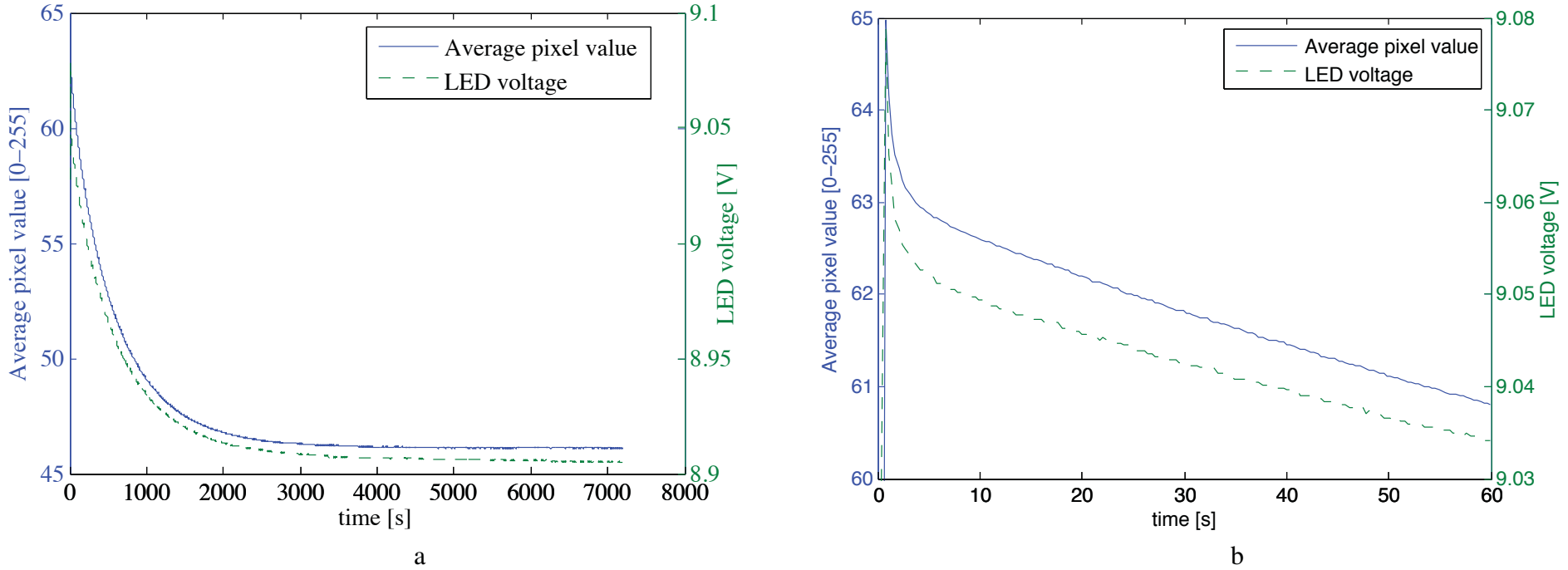

Figure 4.12.: a) Light intensity of Light 3 over an operation time of two hours. As the LEDs warm up, the light intensity decreases. After 3000 seconds, the light reaches the thermal equilibrium. b) Detail of graph a. The Measurement was performed with a camera exposure time of 1/250 s.

5. Implementation of Photometric Stereo

The implementation of the experiment control and the image processing for Photometric Stereo was realized in *Matlab R2008a*. *Matlab* provides utilities for the control of the image Acquisition device, the control of the light sources and advanced matrix operations. This allows a control of the test stand, as well as the data processing on one platform.

5.1. Normalization of Source Images

The idealized model of Photometric Stereo assumes that the irradiance $\mathrm{d}\Phi/\,\mathrm{d}A$ on the surface is equal for all light sources and only the direction of the incident light is changed. This results in a constant factor ρ for all illumination directions in the bidirectional reflectance distribution function (see Section 2.4). However, in a real setup, several factors cause a deviation from an ideal homogeneous illumination:

1. the light sources do not emit collimated light, so that the scene illumination is not homogeneous (see Fig. 5.1 and 4.10);
2. due to fabrication tolerances and varying thermal conditions, the light sources used for the different illumination directions differ in terms of light intensity (see Fig. 6.1);
3. the different positions and therefore distances and orientation of each surface element (x, y) with respect to the light source results in an inhomogeneous light distribution on the surface; and
4. the optical assembly of the camera lens results in a perspective projection, which differs from the assumption of an orthographic imaging device in Section 2.2. The different distance of the camera lens for each surface element (x, y) results in a varying light intensity reaching the camera sensor.

These effects result in a varying reflectance factor ρ for each surface element (x, y) and each illumination direction. This imperfection of a test setup can be compensated by calibration as is shown in the following steps.

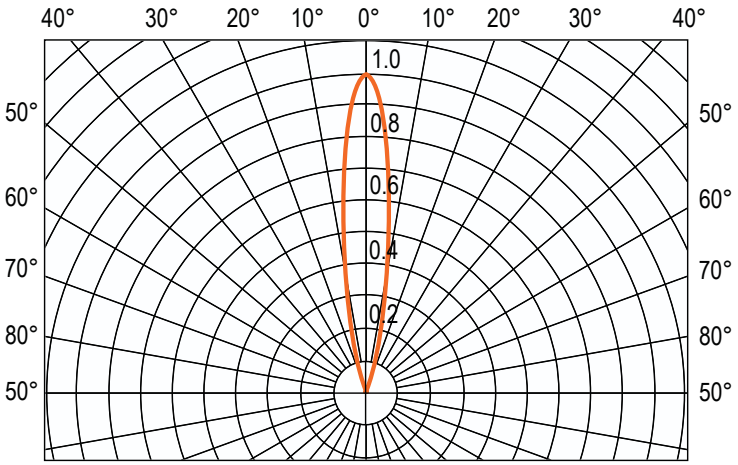

Figure 5.1.: Relative radiation characteristic $I_{rel} = f(\phi)$ of a single Osram Dragoneye LED at temperature $T_a = 25°\mathrm{C}$, according to [10].

Let $\boldsymbol{n} := [\ p_{x,y},\ \ q_{x,y}, 1]^{\mathrm{T}}$ be the normal vector of the surface element (x, y), and $\boldsymbol{s} := [p_{s,x,y}, q_{s,x,y}, 1]^{\mathrm{T}}$ be the vector pointing toward the light source. The intensity for each pixel $(\hat{x}, \hat{y})$ of the corresponding camera image is then given by (see Equation 2.14)

$$I_{\hat{x},\hat{y}} = \rho_{x,y} \underbrace{\frac{(1 \quad p_{x,y}\, p_{s,x,y} \quad q_{x,y}\, q_{s,x,y})}{\sqrt{1 + p_{x,y}^2 + q_{x,y}^2}\,\sqrt{1 + p_{s,x,y}^2 + q_{s,x,y}^2}}}_{\cos(i_{x,y})}, \tag{5.1}$$

where $\rho_{x,y}$ is different for every position (x, y) on the surface. For a calibration object of known shape, Equation 5.1 can be solved for $\rho_{x,y}$. In the following, a white plane paper surface, which offers good Lambertian properties, was used as reference object. Further, let $I^*_{\hat{x},\hat{y}}$ be the raw images of the calibration surface and $\rho^*_{x,y}$ be the reflectance factor for this calibration surface. A plane surface is given by $p_{x,y} = q_{x,y} = 0$ so that

$$I^*_{\hat{x},\hat{y}}\,\sqrt{1 + p_{s,x,y}^2 + q_{s,x,y}^2} = \rho^*_{x,y}\,, \tag{5.2}$$

where $\sqrt{1 + p_{s,x,y}^2 + q_{s,x,y}^2}$ is the reciprocal value of the cosine of the incident angle i. Equation 5.2 can be written as

$$I^*_{\hat{x},\hat{y}} \frac{1}{\cos\left(i_{x,y}\right)} = \rho^*_{x,y}\,. \tag{5.3}$$

Figure 5.2 visualizes the steps for the calculation of $\rho^*_{x,y}$ for the plane paper surface illuminated by Light Source 1.

Figure 5.2.: Calculation of $\rho^*_{x,y}$ from the raw image of the calibration surface. The paper surface was illuminated by Light 1. The arrow depicts the direction of the incident light. The operator $.*$ represents the Hadamard matrix product.

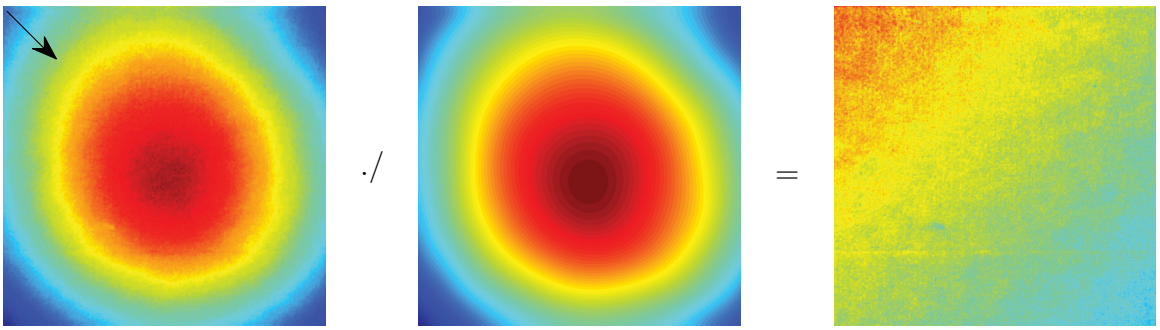

Figure 5.3.: Normalization for the raw image of the calibration surface. The paper surface was illuminated by Light 1. The operator $./$ depicts the Hadamard matrix division.

For a surface of arbitrary shape, the reflectance factor $\rho^*_{x,y}$ for the calibration surface, which contains the information about the scene illumination, can be used to normalize acquired images for use with Photometric Stereo (see Fig. 5.3),

$$I_{n,\hat{x},\hat{y}} := \frac{I_{\hat{x},\hat{y}}}{\rho^*_{x,y}} \; ; \tag{5.4}$$

$$\rho_{n,x,y} := \frac{\rho_{x,y}}{\rho^*_{x,y}} \; . \tag{5.5}$$

Equation 5.1 can now be written as

$$I_{n,\hat{x},\hat{y}} = \rho_{n,x,y} \; \cos\left(i_{x,y}\right) \; . \tag{5.6}$$

This normalization is performed for the images of the four different illumination directions, so that the initial condition for Photometric Stereo of a constant ρ for each pixel and for all light sources is fulfilled,

$$I_{n,1,\hat{x},\hat{y}} = I_{1,\hat{x},\hat{y}}/\rho^*_{1,x,y} = \rho_{n,x,y}\ \cos\left(i_{1,x,y}\right)\ ; \tag{5.7}$$

$$I_{n,2,\hat{x},\hat{y}} = I_{2,\hat{x},\hat{y}}/\rho^*_{2,x,y} = \rho_{n,x,y}\ \cos\left(i_{2,x,y}\right)\ ; \tag{5.8}$$

$$I_{n,3,\hat{x},\hat{y}} = I_{3,\hat{x},\hat{y}}/\rho^*_{3,x,y} = \rho_{n,x,y}\ \cos\left(i_{3,x,y}\right)\ ;\ and \tag{5.9}$$

$$I_{n,4,\hat{x},\hat{y}} = I_{4,\hat{x},\hat{y}}/\rho^*_{4,x,y} = \rho_{n,x,y}\ \cos\left(i_{4,x,y}\right)\ . \tag{5.10}$$

For a surface with the same ideal Lambertian reflectance characteristic as the calibration surface, $\rho_{n,x,y}$ is equal to 1. The results of the normalization are shown in Section 6.

The normalized images are used as input pictures for the method of Photometric Stereo (see Section 5.2). The raw image of the calibration surface and the corresponding normalized image can be compared in Fig. 6.1 and Fig. 6.6. The implementation of the calibration in Matlab is shown in Section A.1.

5.1.1. Filtering the Calibration Matrix

The raw pictures for calibration $I_{1,\hat{x},\hat{y}}$ - $I_{4,\hat{x},\hat{y}}$ show the roughness of the paper calibration surface. The small unevenness of the surface does not meet the initial assumption of an ideal plane surface and therefore results in an error. In order to eliminate this noise, $\rho^*_{1,\hat{x},\hat{y}}$ - $\rho^*_{4,\hat{x},\hat{y}}$ were filtered by fitting a polynomial function $\bar{\rho}^*_{1,\hat{x},\hat{y}}$ - $\bar{\rho}^*_{4,\hat{x},\hat{y}}$ through the intensity values of each pixel $(\hat{x},\hat{y})$ (see Fig. 5.4 and 6.4). This polynomial function is free of noise and has an insignificant deviation from the unfiltered matrix (see Fig. 6.5). The fitting was performed using the method of discrete polynomial moments (see [9]).

5.2. Calculation of the Gradient Field

The method of Photometric Stereo needs to be adapted to the specific design of the test stand. Equation 3.10 is expanded to use four instead of the minimum of three illumination directions. The equation then has the form

$$\underbrace{\begin{bmatrix} I_{n,1} \\ I_{n,2} \\ I_{n,3} \\ I_{n,4} \end{bmatrix}}_{\tilde{\boldsymbol{I}}_n} = \rho_n \underbrace{\begin{bmatrix} s_{11} & s_{12} & s_{13} \\ s_{21} & s_{22} & s_{23} \\ s_{31} & s_{32} & s_{33} \\ s_{41} & s_{42} & s_{43} \end{bmatrix}}_{\tilde{\mathsf{N}}} \underbrace{\begin{bmatrix} n_1 \\ n_2 \\ n_3 \end{bmatrix}}_{\tilde{\boldsymbol{n}}} . \tag{5.11}$$

This equation is solved in the least squares sense such that

$$\tilde{\boldsymbol{n}} = \frac{1}{\rho_n}\tilde{\mathsf{N}}^{+}\tilde{\boldsymbol{I}}_n\ , \tag{5.12}$$

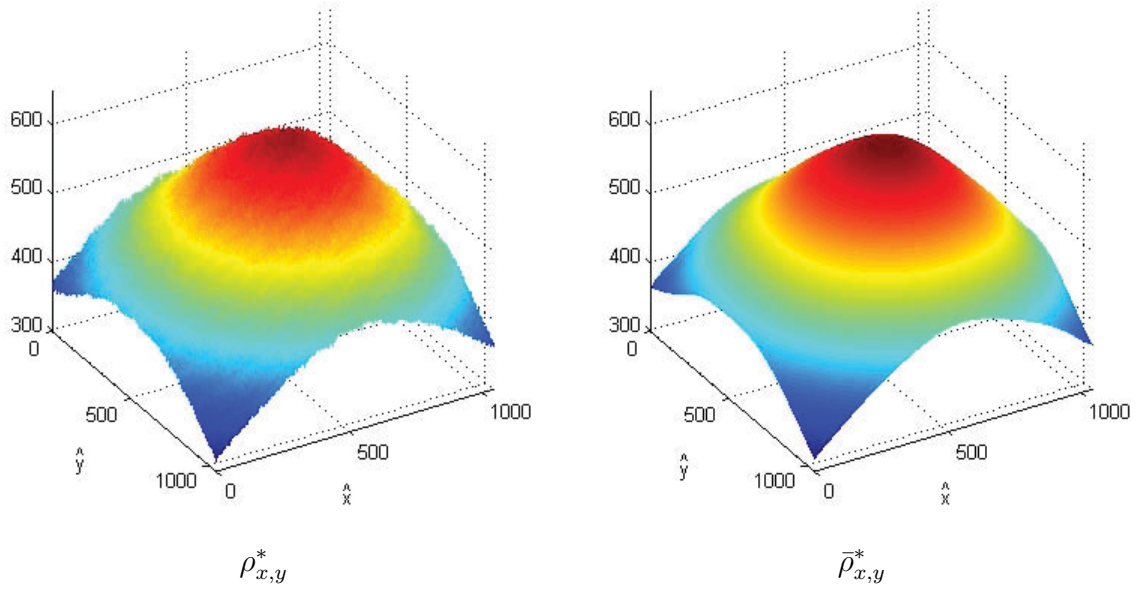

$\rho^*_{x,y}$ $\bar{\rho}^*_{x,y}$

Figure 5.4.: Surface view of calibration matrix $\rho^*_{x,y}$ for Light 1. The roughness of the calibration object causes visible noise; $\bar{\rho}^*_{x,y}$: the polynomial function of degree 10 suppresses the noise effectively.

where $\tilde{\mathsf{N}}^+ = \left(\tilde{\mathsf{N}}^{\mathrm{T}}\tilde{\mathsf{N}}\right)^{-1}\tilde{\mathsf{N}}^{\mathrm{T}}$ is the Moore-Penrose pseudoinverse of $\tilde{\mathsf{N}}$ [1].

In order to determine the gradient field of the surface, Equation 5.12 is individually solved for each pixel of the camera image,

$$\tilde{\boldsymbol{n}}_{x,y} = \frac{1}{\rho_{n,x,y}}\tilde{\mathsf{N}}^+_{x,y}\tilde{\boldsymbol{I}}_{n,\hat{x},\hat{y}} \ . \tag{5.13}$$

The incident angle i is different for each pixel $(\hat{x}, \hat{y})$ so that $\tilde{\mathsf{N}}$ needs to be formed for each position in the image. For a well defined setup, where the position of the light sources relative to the global coordinate is known, the $\tilde{\mathsf{N}}_{\hat{x},\hat{y}}$ can be formed and the according Moore-Penrose pseudoinverse $\tilde{\mathsf{N}}^+_{\hat{x},\hat{y}}$ can be calculated. This is computationally the most expensive part of the image processing. For a test stand with static light sources and a known geometry, this calculation can be done and the matrices stored a-priori. During the actual survey, the gradient field of the surface is then calculated by simple matrix-vector multiplications - a significant contribution to the performance of the algorithm. The Matlab-code for the calculation of $\tilde{\mathsf{N}}_{\hat{x},\hat{y}}$ is shown in Section A.2, and the implementation for calculating the gradient field in Section A.3.

The normalized reflectance factor $\rho_{n,x,y}$ in Equation 5.13 is supposed to be 1 for each (x, y) because of the normalization of the input images described in Section 5.1. This assumption holds for materials with ideal Lambertian reflectance properties such as the paper calibration surface. However, for materials that combine Lambertian with specular or absorbent optical properties, $\rho_{n,x,y}$ can have different values. In Equation 3.12, it is shown that the normalized

reflectance factor can be calculated for each pixel as $\rho_{n,x,y} = \left|\tilde{\mathsf{N}}_{x,y}^{-1}\tilde{\boldsymbol{I}}_{n,\hat{x},\hat{y}}\right|$. The aberration of $\rho_{n,x,y}$ from 1 is an indicator for the validity of the Lambertian Reflectance Model for the surface patch (x, y). Furthermore, the homogeneity of the surface material is shown.

5.3. Systematic Errors

5.3.1. Inhomogeneous Illumination and Projective Geometry

In Section 5.1 it is shown that the light intensity reaching a camera pixel is a function of the orientation of the surface and of the reflectance factor,

$$I = f(p, q, \rho) = f\left(\frac{\partial z}{\partial x}, \frac{\partial z}{\partial y}, \rho\right) . \tag{5.14}$$

This assumption presumes that the incident light is collimated and the image acquisition device uses an orthographic projecting lens. However, in a real test setup, the light sources are inhomogeneous point sources and the camera lens images with perspective projection. The calibration described in Section 5.1 assumes that the center of each surface element lies in a well defined plane in which the calibration was performed. When the surface element is displaced in the z-direction, the impinging light intensity changes. Additionally, the surface element (x, y) is not mapped to the pixel $(\hat{x}, \hat{y})$ anymore (see Fig. 5.5). The light intensity is then a function of

$$I = f\left(z, \frac{\partial z}{\partial x}, \frac{\partial z}{\partial y}, \rho\right) . \tag{5.15}$$

This differential equation does not allow a calculation of the surface gradient as described in Section 3.1 by simple matrix operations. For a solution, the spatial distribution of the illumination, as well as the projection mode of the camera, needs to be known. However, for a surface with small surface features and a sufficient distance from the camera and light source to the surface, the error is insignificant. Because of the additional unknown data, as well as the higher computational effort, the solution of Equation 5.15 was not further investigated.

5.3.2. Shading

Another error occurs if the slope of a surface patch is greater than the angle of the incident light on the surface. In this case, a part of the surface is shaded and the calculation of the surface gradient delivers incorrect results. Generally the method of Photometric Stereo is not applicable to surface patches with a higher slope than the angle w (see Fig. 4.2). To avoid shading, the angle w can be increased by repositioning the light sources. Another option is to install additional light sources so that illumination cases where shading appears can be ignored in the calculation. However, discontinuities cannot be resolved using Photometric Stereo.

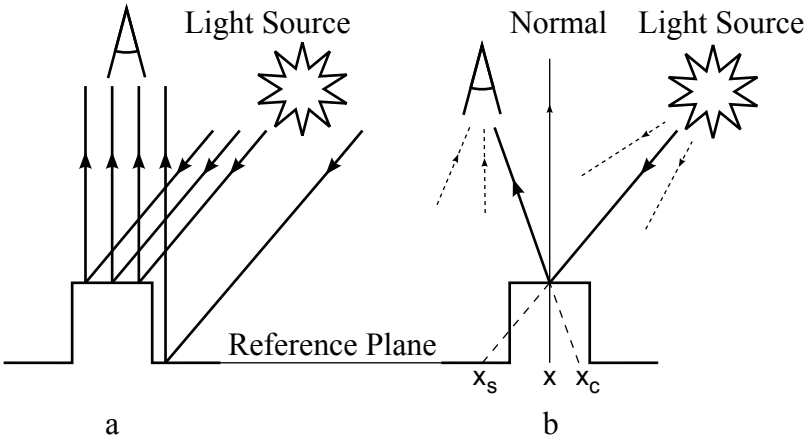

Figure 5.5.: Error caused by inhomogeneous illumination and perspective projection of the camera: a) ideal case of collimated light and orthographic projection: the light intensity reaching the surface is independent of the position of the surface element. Each pixel of the orthographic camera observes the exact underlying surface element; b) inhomogeneous illumination and perspective camera projection: the surface element at the position x receives the light intensity of the surface element x_s. The camera maps the surface element x on the position of the element x_c.

5.3.3. Internal and Multiple Reflections

Internal and multiple reflections appear in surface dents. Diffuse light reflected from one surface patch impinges on another area of the surface so that this area appears brighter (see Fig. 5.6). The increase of light intensity received by the camera is not related to the gradient of the observed surface patch and results in an error.

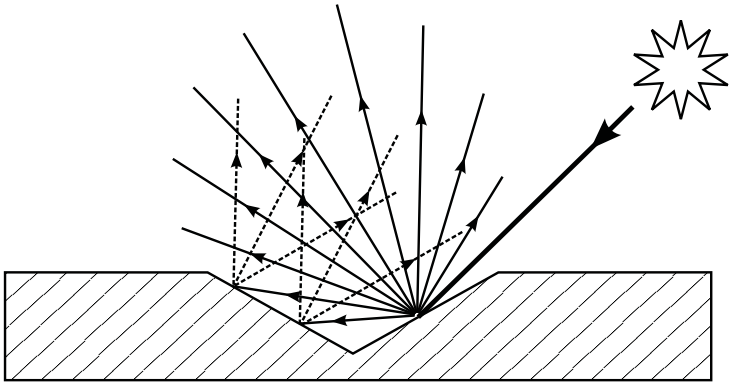

Figure 5.6.: Internal reflection of a light ray in a surface dent.

5.4. Computational Performance

The image processing for Photometric Stereo can be divided into three parts:

1. calibration of the setup;
2. calculation of the gradient field; and
3. surface reconstruction from the gradient field.

$\tilde{\mathsf{N}}^{+}_{x,y}$ and $\bar{\rho}_{x,y}$ only depend on the geometry of the test setup and the illumination conditions. After an initial calibration with the reference surface these matrices can be stored. This is the computationally most expensive part of the implementation.

The calculation of the gradient field is done by simple element-wise matrix multiplications. Using matrix operation capabilities provided by Matlab, the computation can be performed without iterative code: this is a critical benefit for the code performance. The computation of the gradient field in double precision from four input images with a resolution of 1040x1040 pixels took 1.6 seconds on an *Intel Core 2 Duo T6300* System with 1024MB memory.

6. Calibration of the Experiment Setup

The calibration of the test setup was performed according to Section 5.1. A calibration surface of plane white paper was used, which offered ideal Lambertian reflectance. The paper was fixed at a distance of 10 millimeters above the specimen stage, so that the paper was at the same level as the surface of the metal specimen surveyed in Section 7. The results of the calibration can be seen in Figure 6.1 - 6.5.

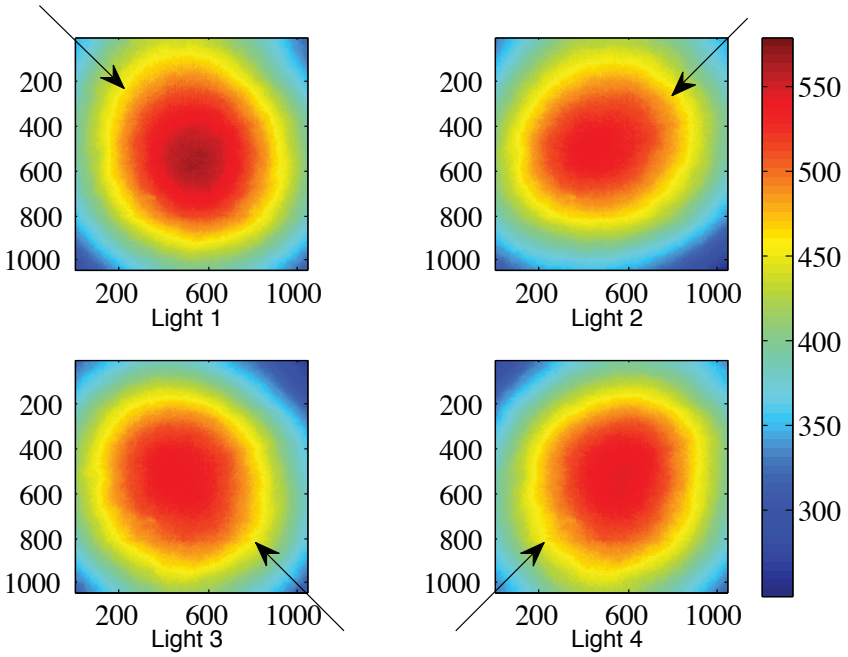

Figure 6.1.: Source images $I^*_{\hat{x},\hat{y}}$ of Light Sources 1-4 for a plane calibration surface ($p_{x,y} = q_{x,y} = 0$). The arrows indicate the direction of the incident light. The material of the test surface is white planar paper, which offers ideal Lambertian reflectance, but shows a significant roughness. The pictures are acquired with an exposure time of 1/125 s, but are extrapolated to an exposure time of 1/30 s.

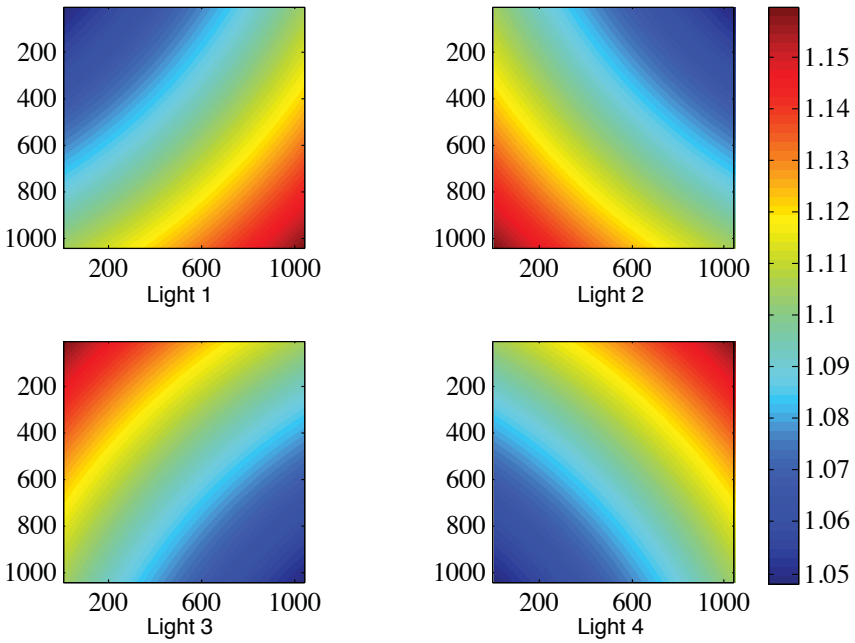

Figure 6.2.: Reciprocal cosine of the incident angle i for each position $(\hat{x}, \hat{y})$ in each image. The incident angle i depends on the position of the light source, so that for each light source a different matrix is generated.

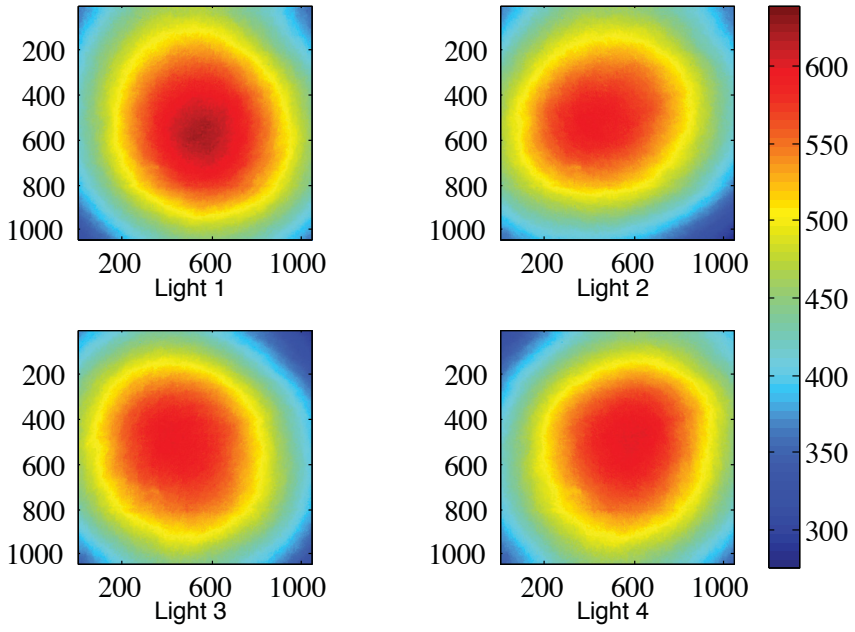

Figure 6.3.: Reflectance factor $\rho^*_{\hat{x},\hat{y}}$ for Light Sources 1-4 calculated from source images in Figure 6.1 and geometric information from Figure 6.2. The pictures show the surface roughness of the paper used for calibration.

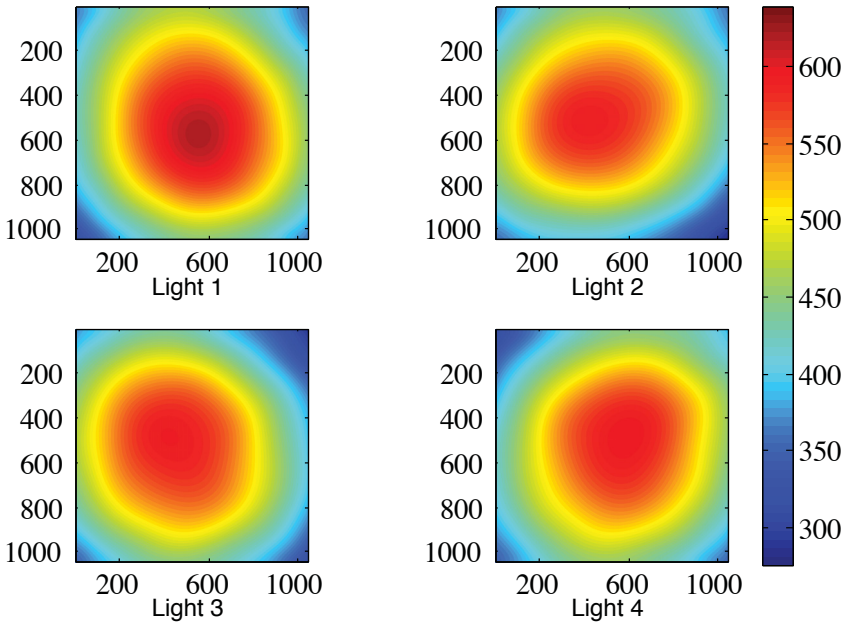

Figure 6.4.: Calibration factor $\bar{\rho}^*_{\hat{x},\hat{y}}$ for Light Sources 1-4. The filtering of $\rho^*_{\hat{x},\hat{y}}$ was achieved by fitting a polynomial function of degree 10 in both the $\hat{x}$- and $\hat{y}$-directions to the original image.

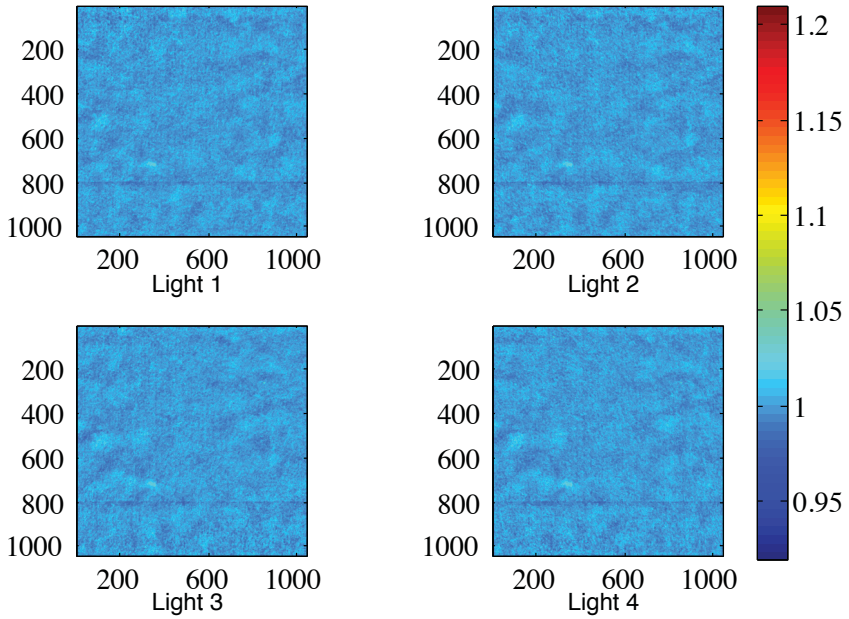

Figure 6.5.: Proportion of filtered and original reflectance factor $\bar{\rho}^*_{\hat{x},\hat{y}}/\rho^*_{\hat{x},\hat{y}}$. The polynomial function of degree 10 in $\hat{x}$- and $\hat{y}$-directions approximates the original reflectance factor while filtering the noise.

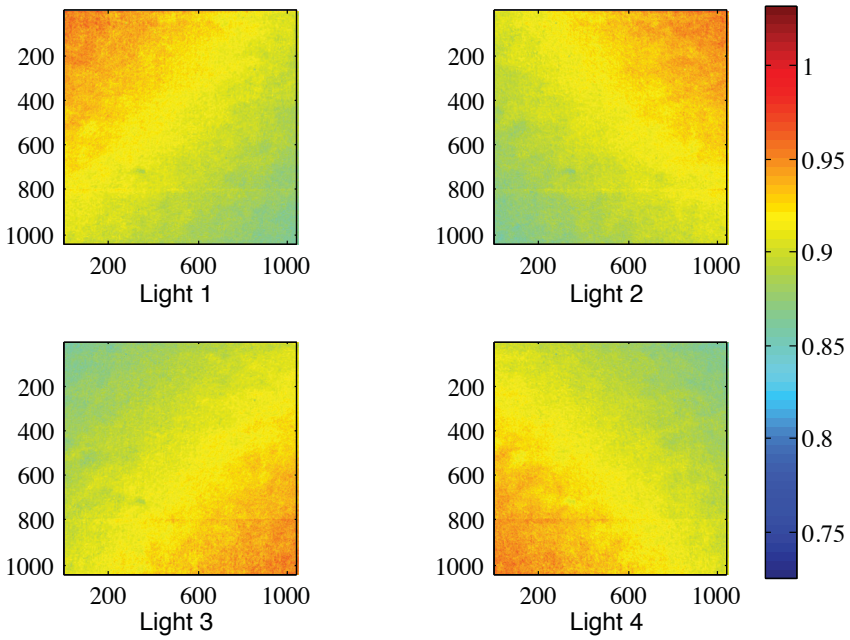

Figure 6.6.: Normalized pictures $I^*_{n,x,y}$ of the calibration surface. The inhomogeneous light distribution of the source pictures from Figure 6.1 is compensated. The remaining gradient in the pictures is due to the changing angle of the incident light. The noise is caused by the paper roughness.

The verification of the calibration procedure is performed by applying Photometric Stereo to the images of the calibration surface; in the first step, the images acquired for calibration (Figure 6.1) are normalized with the calibration matrix in Figure 6.4. The result of this normalization is shown in Figure 6.6. Next the surface gradient is calculated with Photometric Stereo and the surface is reconstructed. The following expectations for the result can be made:

1. the normalized reflectance factor ρ_n is 1 for all points $(\hat{x}, \hat{y})$ (see Fig. 6.7);
2. the gradients p and q are equal to zero for all points $(\hat{x}, \hat{y})$ (see Fig. 6.8);
3. the surface is flat, thus the surface height is zero for all points $(\hat{x}, \hat{y})$ (see Fig. 6.9).

These expectations are true for ideal conditions. However, the waviness and roughness of the calibration surface were filtered from the calibration matrix $\bar{\rho}_{\hat{x},\hat{y}}$ and thus not accounted for in the calibration procedure. These characteristics of the surface left a residual in the surface gradient field, the normalized reflectance factor and the reconstructed surface. However, another source for the residual can be an inhomogeneity of the illumination of a higher degree than the polynomial filtering of the calibration matrix.

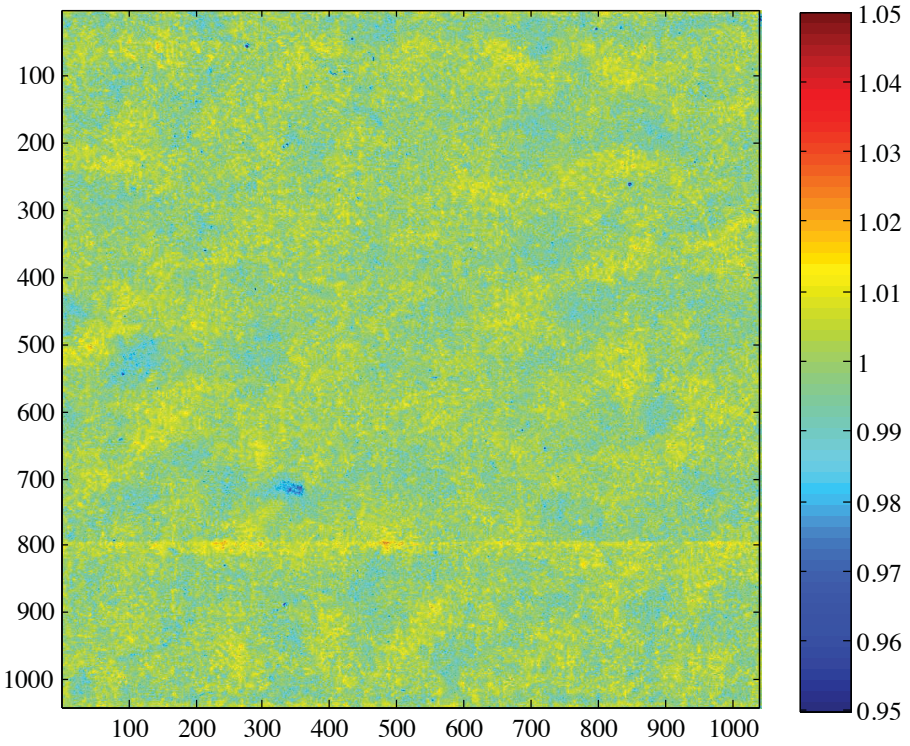

Figure 6.7.: Normalized reflectance factor $\rho_{n,\hat{x},\hat{y}}$ for the calibration surface calculated with Photometric Stereo. The horizontal line in the image at $\hat{y} = 800$ is caused by an error of the camera sensor.

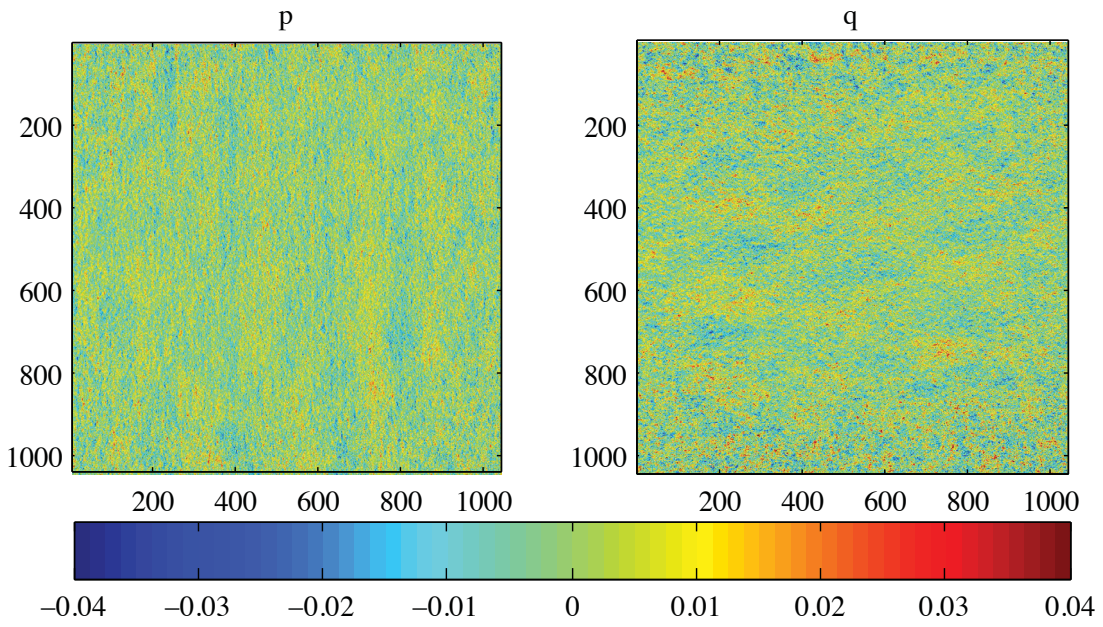

Figure 6.8.: Gradient field of the calibration surface calculated with Photometric Stereo.

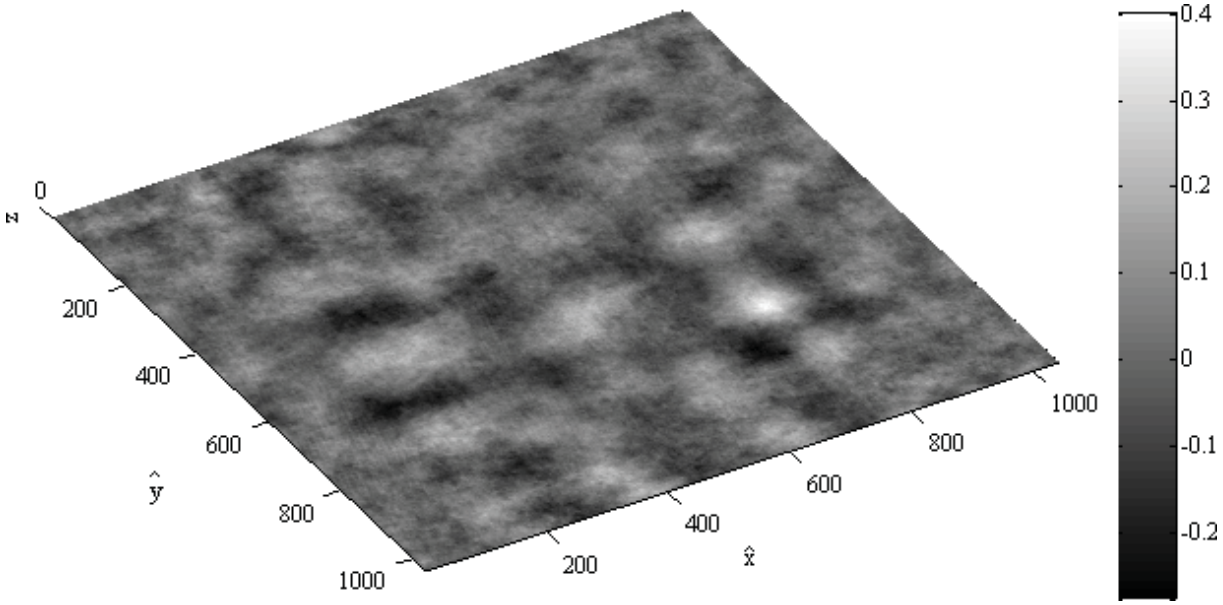

Figure 6.9.: Reconstructed surface for the calibration surface calculated with Photometric Stereo. The maximum error in the reconstruction is 0.7 pixels. This error is smaller than the initial resolution of the image and can be neglected.

6.1. Evaluation of the Calibration

The correct adjustment and calibration of the experiment setup was evaluated by performing a series of tests with the calibration surface. The paper was positioned on the specimen stage and tilted in different directions so that its surface normal vector $\boldsymbol{n}$ formed an angle of 5° with the z-axis. The method of Photometric Stereo was applied for each case and the calculated gradient field and the reconstructed surface were evaluated. Table 6.1 shows the different orientations of the surface used for the evaluation.

Scenario	Rotation axis	Rotation angle	Resulting $\boldsymbol{n}$
1	$[0\ 1\ 0]^{\mathrm{T}}$	-5°	$[tan\,(-5^\circ)\,, 0, 1]^{\mathrm{T}}$
2	$[1\ -1\ 0]^{\mathrm{T}}$	5°	$\left[-tan\,(5^\circ)\,/\sqrt{2}, -tan\,(5^\circ)\,/\sqrt{2}, 1\right]^{\mathrm{T}}$
3	$[1\ 0\ 0]^{\mathrm{T}}$	5°	$[0, -tan\,(5^\circ)\,, 1]^{\mathrm{T}}$

Table 6.1.: Test Scenarios for evaluation of the calibration. The table shows the analytical solution for the surface normal vector $\boldsymbol{n}$ as result of the rotation of the paper surface.

The analytical solution for the surface normal vector in Table 6.1 allows the calculation of the analytical surface gradient (p, q) for each scenario. The surface normal vector is defined as $\boldsymbol{n} := [-p, -q, 1]^{\mathrm{T}}$. Table 6.2 shows the numerical values of the gradient for each test scenario.

Scenario	p	q
1	0.087	0
2	0.062	0.062
3	0	0.087

Table 6.2.: Numerical gradient.

The analytical values and the measured gradient fields are compared in Figure 6.10. The pictures show that the measured gradient fields are inhomogeneous and differ significantly from the analytical value. The reason for this error is the inhomogeneous illumination (see Section 5.3). The calibration for a surface patch is performed for it's specific location at (x, y, z). If the surface patch is displaced in the direction of the z-axis, it is illuminated with a different light intensity than estimated during the calibration. This effect can be seen in Figure 6.11. The optical properties of the paper surface match the properties of the calibration surface so that the normalized reflectance factor $\rho_{n,\hat{x},\hat{y}}$ is expected to equal 1. Surface patches displaced in z-direction show an error of ρ_n. Patches with decreased distance to the light source receive a higher light intensity and show a positive error, whereas patches with increased distance to the light source show a negative error. Patches lying in the rotation axis only change the surface normal vector and show a normalized reflectance factor of $\rho_n = 1$.

The surfaces reconstructed from the gradient fields for Scenarios 1-3 are shown in Figure 6.12. The cross sections of these surfaces in Figure 6.13 - 6.15 show that the surface reconstruction produces a small error. The reconstructed surfaces are not perfectly plane and show a convex error.

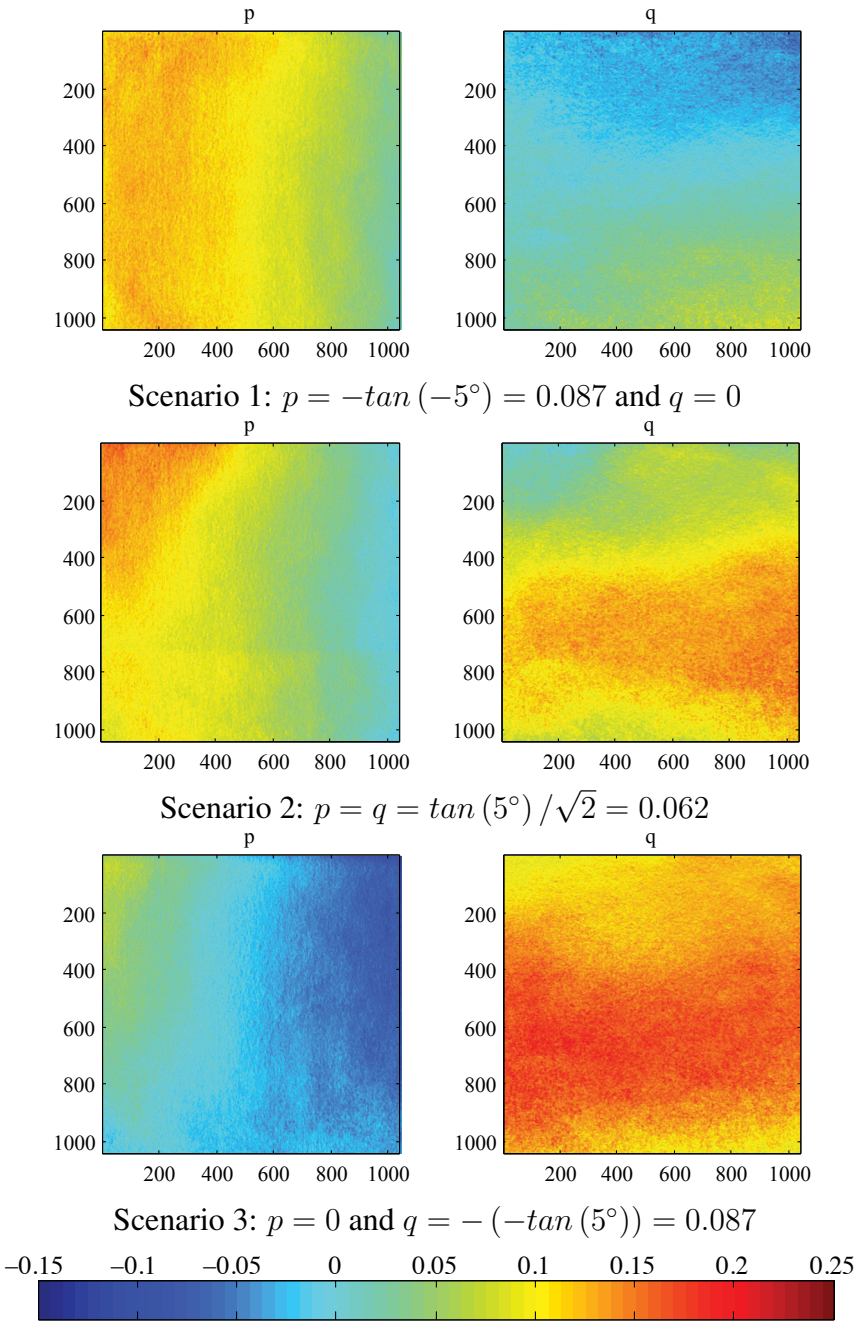

Figure 6.10.: Gradient field of the tilted surface for each test scenario. The analytical values for the gradients are given for each scenario.

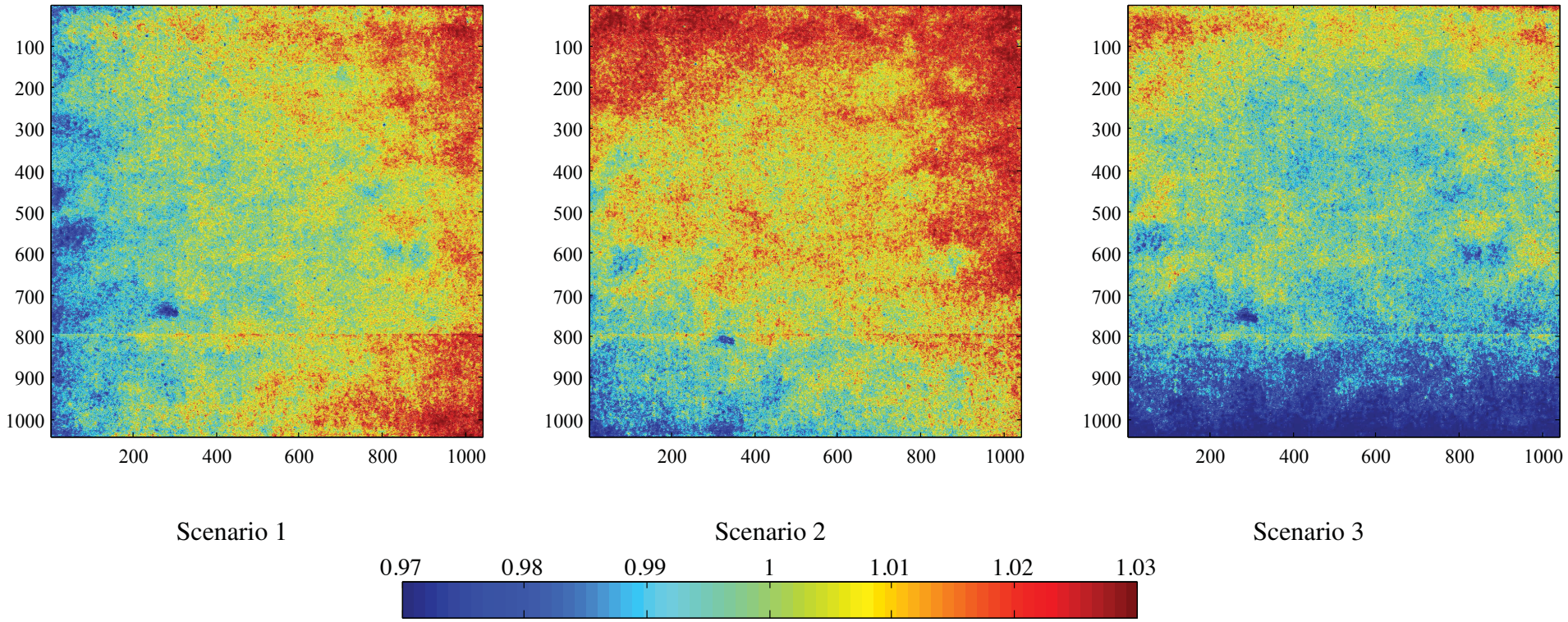

Figure 6.11.: Normalized reflectance factors $\rho_{n,\hat{x},\hat{y}}$ for Scenarios 1-3. Because of the ideal Lambertian reflectance characteristic of the specimen, the normalized reflectance factor is expected to equal 1. However, when a surface patch $(\hat{x}, \hat{y})$ is displaced in the direction of the z-axis, the calibration is incorrect so that the according ρ_n is different from 1 (see Section 5.3). The greater the distance of a surface patch is from the rotation axis, the greater the displacement in the z-direction and the greater is the error of ρ_n.

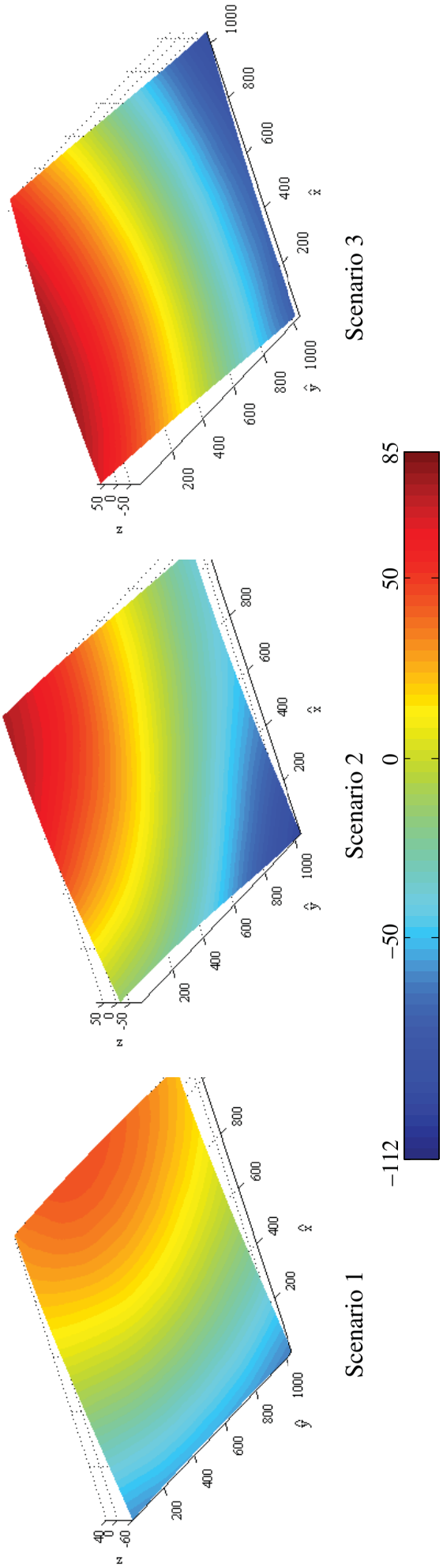

Figure 6.12.: Surfaces reconstructed from the gradient fields. The surfaces appear slightly convex.

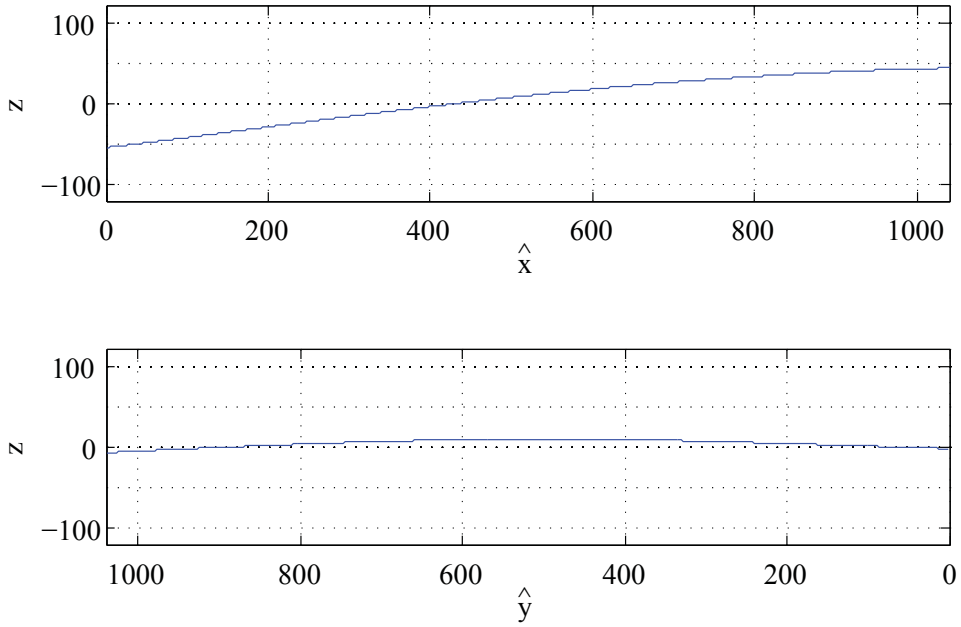

Figure 6.13.: Cross section of the reconstructed surface for Scenario 1 at $\hat{y} = 520$ (upper graph) and $\hat{x} = 520$ (lower graph).

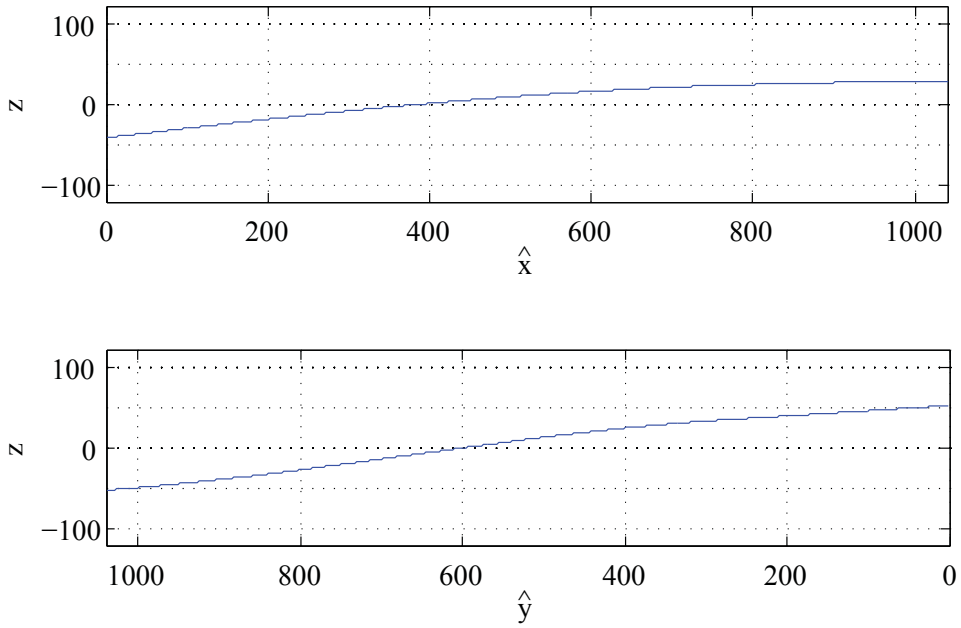

Figure 6.14.: Cross section of the reconstructed surface for Scenario 2 at $\hat{y} = 520$ (upper graph) and $\hat{x} = 520$ (lower graph).

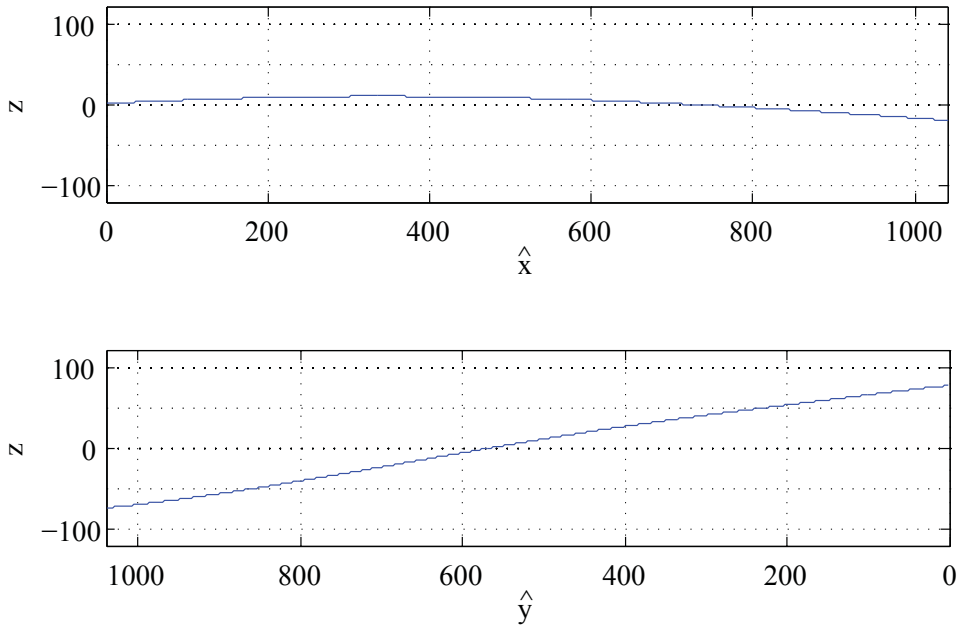

Figure 6.15.: Cross section of the reconstructed surface for Scenario 3 at $\hat{y} = 520$ (upper graph) and $\hat{x} = 520$ (lower graph).

7. Photometric Stereo Applied to a Metallic Surface

The use of Photometric Stereo as a surface inspection method in industrial application is mainly limited by the optical properties of the test specimen. Section 6 shows the application of Photometric Stereo to a Lambertian surface with simple geometry. In this chapter, Photometric Stereo is applied to a metal surface.

In steel mills, semi-finished products such as bars or slabs are marked so that they can be identified by the process-monitoring system. The high temperature of the material and environmental conditions, such as dust and vapor, require a robust label. This is achieved by stamping a numerical code as numbers and as bar code into the surface of the bar. The end of a steel bar with embossed label is shown in Figure 7.1. The surface of this steel bar has a rough structure and is partially covered with oxide scale. The process of hammering the label onto the surface removes the scale from the area around the code so that the base material became visible (see Fig. 7.2). While the oxide scale appears glossy, the underlying steel has a diffuse reflectance characteristic.

7.1. Reflectance Characteristic of the Metal Specimen

The method of Photometric Stereo is based on the Lambertian Reflectance Model (see Eq. 2.5). The calculation of the gradient field produces an error if the surface has a different reflectance characteristic. For this reason, the reflectance characteristic of the metal bar was determined by measuring the reflected light intensity of a plane steel surface. This surface was of the same alloy and was processed the same way as the specimen described in Section 7. The optical properties of the surface equaled the properties of the base material of the specimen.

The measurement was performed by positioning the camera above the surface and surveying the reflected light intensity. The direction of the incident light was changed in one-degree steps while keeping the distance between the light source and the surface constant (see Figure 7.3). According to Equation 2.5, the reflected light intensity is proportional to the cosine of the incident angle. Figure 7.4 shows the result of the measurement. The curve approximates a line so that the surface is well described by the Lambertian Reflectance Model. This evaluation was not performed for the oxide scale. However, its clearly visible glossy characteristic infers that the Lambertian Law is not applicable to the scale.

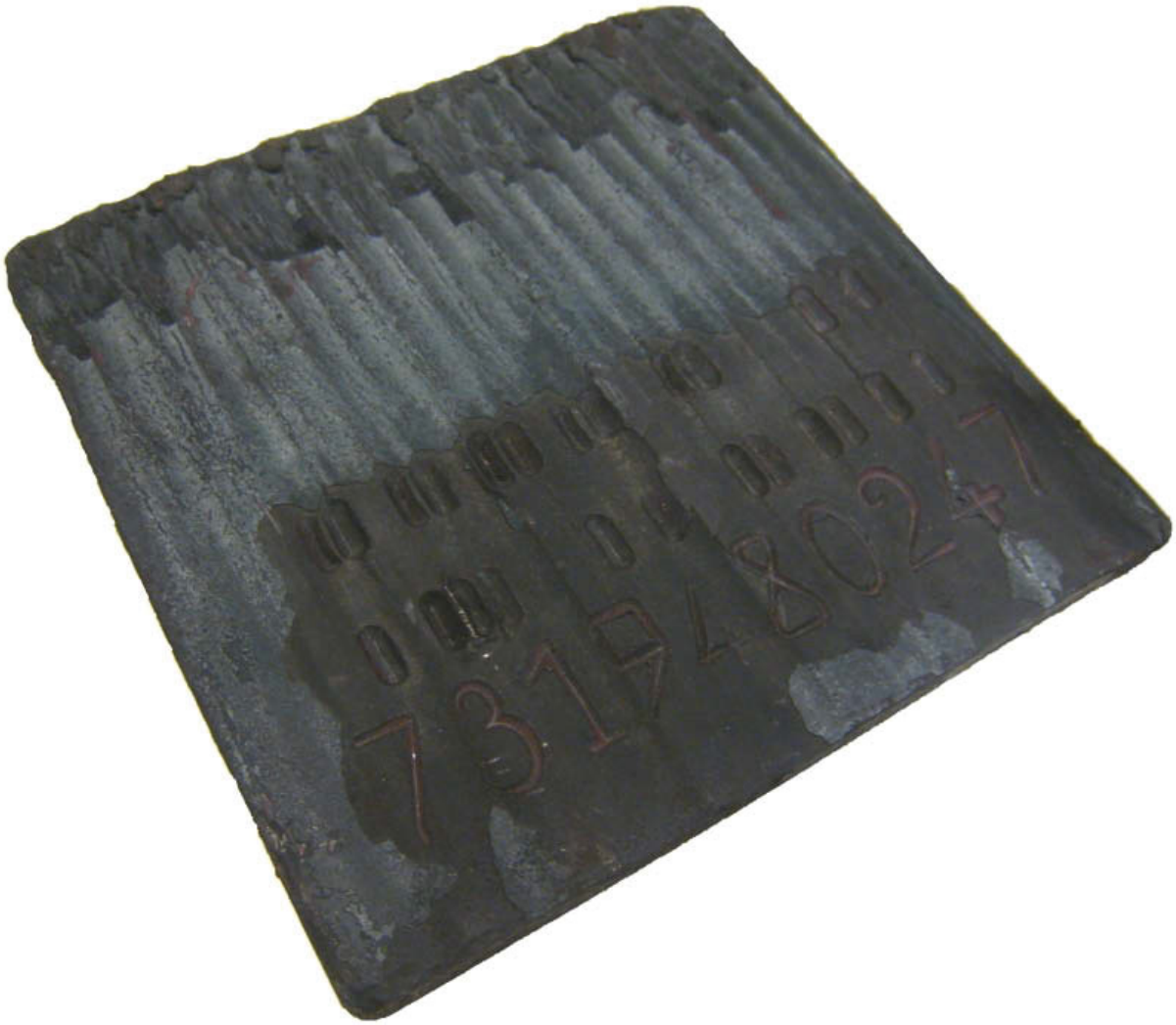

Figure 7.1.: Cut off end of a steel bar with embossed identification code. The surface shows grooves parallel to the left and right edge. The area in the top half is covered by oxide scale. In the label area, the scale chipped off during the stamping process. The square block has an edge length of 175 mm and a height of 10 mm.

Figure 7.2.: Detail of Figure 7.1: transition between oxide scale and base material. The scale appears glossy, the underlying steel diffuse.

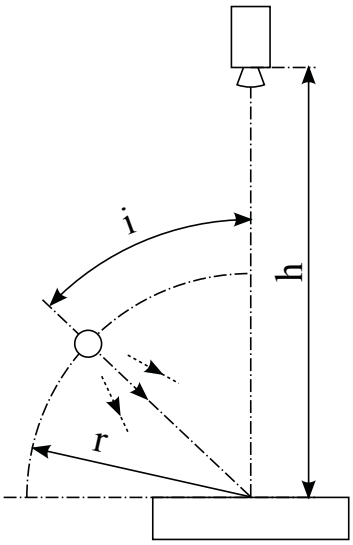

Figure 7.3.: Setup for the measurement of the reflectance behavior of steel. The camera measures the reflected intensity of the metal surface while the angle i of the incident illumination is increased in one degree steps. The distance h between camera and surface was chosen to be 100 cm and the distance between light source and surface r to be 33 cm.

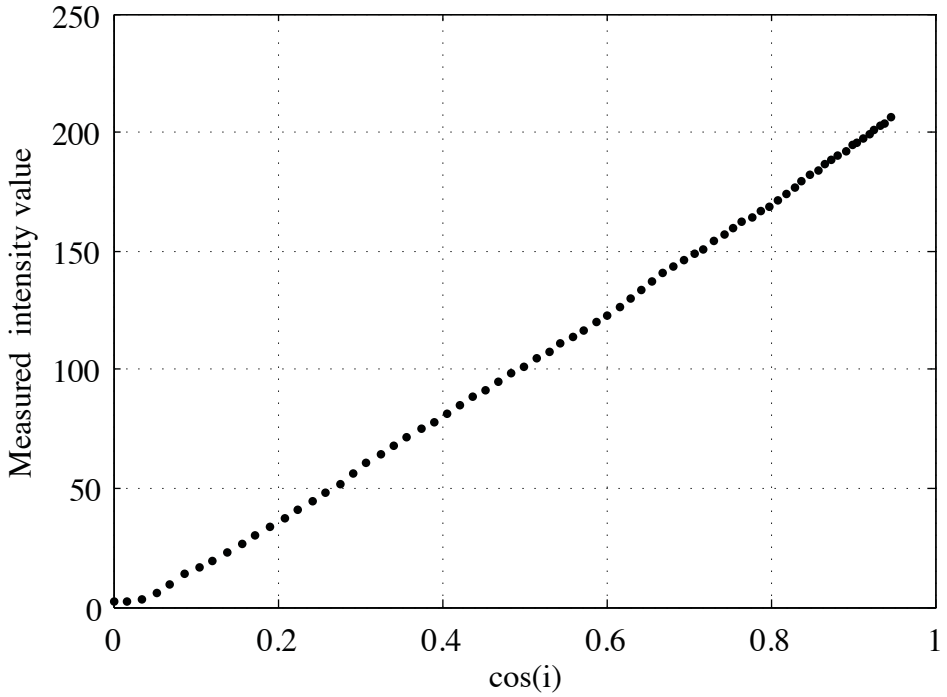

Figure 7.4.: Reflectance behavior of a steel block: measured intensity versus the cosine of the incident angle i. The data points lie close to a line, so that the Lambertian Reflectance Model describes the surface's optical properties sufficiently.

7.2. Surface Reconstruction of the Metallic Surface

The normalized surface reflectance factor $\rho_{n,\hat{x},\hat{y}}$ in Figure 7.5 shows the different reflectance characteristics of the oxide scale and the base material. The area with the metal scale shows a significantly higher reflectance than the base material. Figure 7.5 shows also a systematic error of the test setup: for an ideal Lambertian surface, $\rho_{n,\hat{x},\hat{y}}$ would be constant over the whole picture; however, the bar code, as well as the numbers and grooves are clearly visible in the figure. This effect is due to the inhomogeneous illumination and the errors described in Section 5.3.

The calculation of the surface gradient field demonstrates the effect of the different characteristics of the metallic surface. The grooves on the surface are in direction of the y-axis. While the depth of the grooves on the specimen remains constant in y, Figure 7.6 shows an increased gradient p for the grooves in the area covered by scale.

The surface reconstructed from the gradient field falls in the x- and y-directions. This error was observed for all tested metal surfaces and appears to be systematic. The error results from the inaccurately determined surface gradient and is amplified by the numerical integration.

In an attempt to compensate the error, a two-dimensional polynomial surface $P_{\hat{x},\hat{y}}$ of degree two was fitted to the surface $Z_{\hat{x},\hat{y}}$ (see Figure 7.8) using the method of discrete polynomial moments [9]. The residual of the correction of the reconstructed surface with the polynomial fit is shown in Figure 7.9. The escalated gradient observed in Figure 7.6 for the area covered by oxide scale results in significantly higher grooves in this area. Generally, the reconstructed surface shows higher waviness than the original metal surface.

The reconstructed surface provides the data for further image processing. In order to read the bar code, the depth information of the label needs to be separated from the wavy base material. The low accuracy of the reconstructed surface shows that the current method of Photometric Stereo is only a tool for qualitative feature detection. For materials with Lambertian reflectance characteristic and small height deviations from the reference plane, features can be detected in a robust manner. For glossy surfaces, the accuracy of the method decreases significantly with the increase of the specular fraction of the reflection.

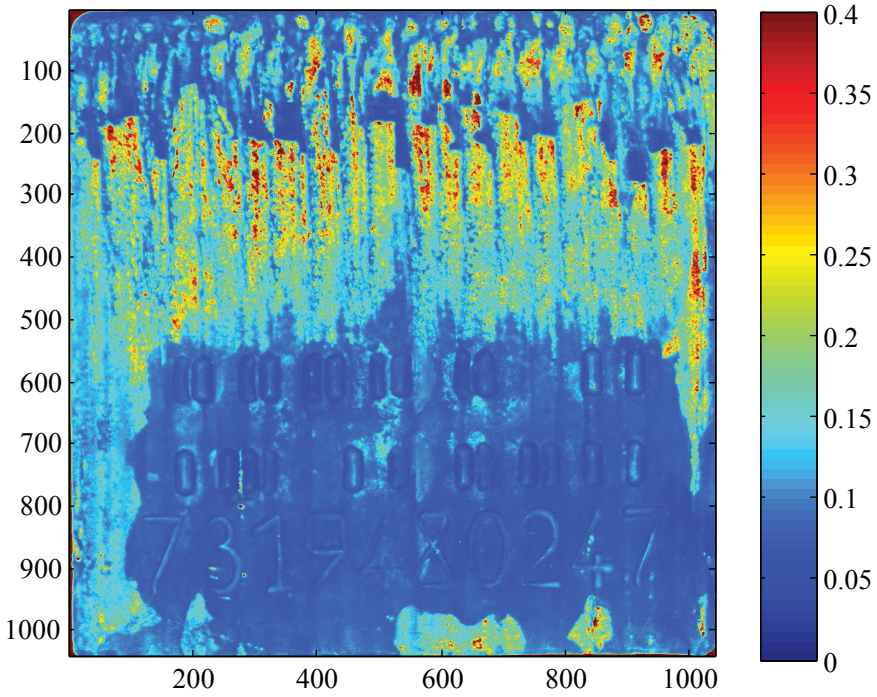

Figure 7.5.: Normalized reflectance factor $\rho_{n,\hat{x},\hat{y}}$ for the metal surface. The difference of the reflectance characteristic between oxide scale and base material is clearly visible.

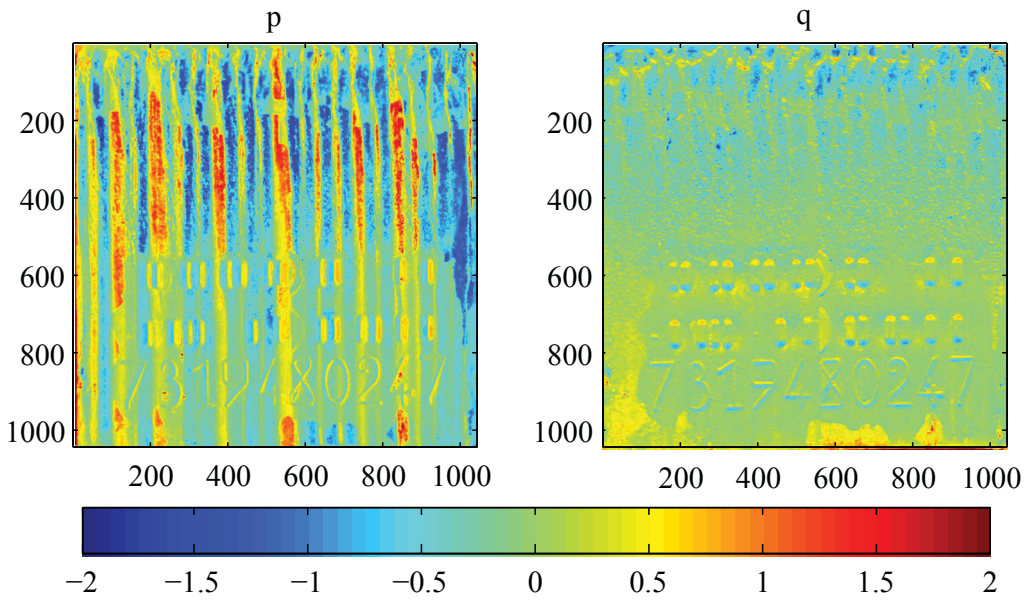

Figure 7.6.: The calculated gradient field of the metal surface shows the different reflectance characteristics of oxide scale and the base material. The area in the top half of the picture is covered with scale, the value of p calculated with Photometric Stereo is significantly higher than for the base material.

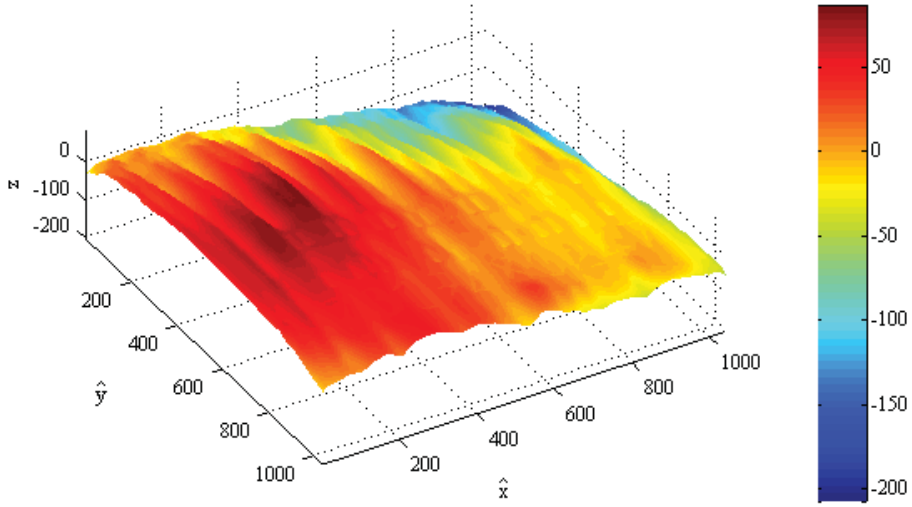

Figure 7.7.: Reconstructed Surface $Z_{\hat{x},\hat{y}}$ from gradient in Figure 7.6. The surface falls in $\hat{x}$ and $-\hat{y}$-direction.

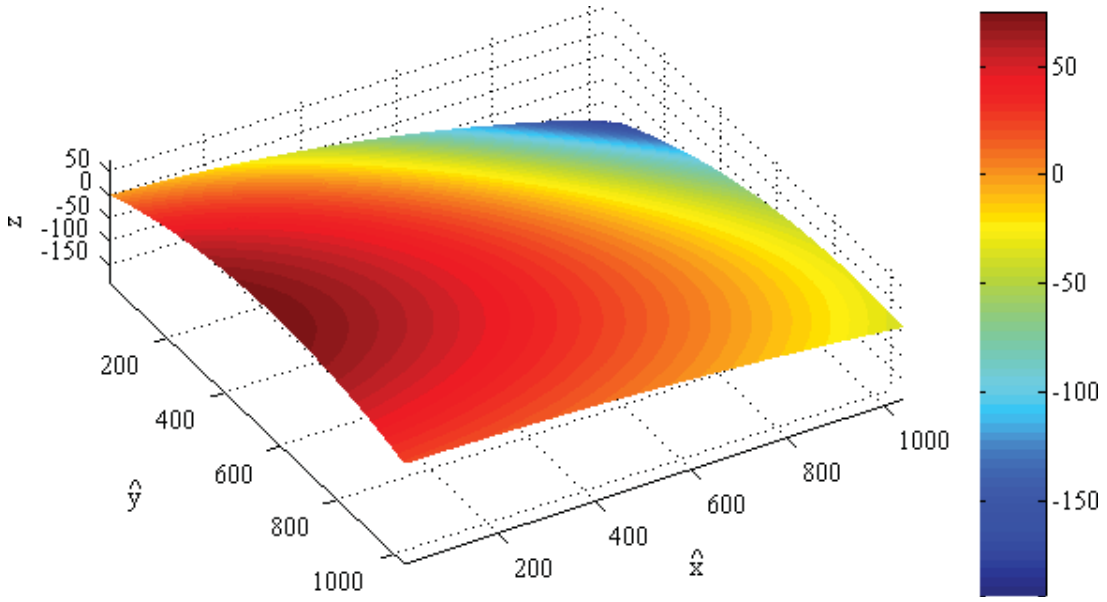

Figure 7.8.: Polynomial fit $P_{\hat{x},\hat{y}}$ of degree two for the reconstructed surface in Figure 7.7.

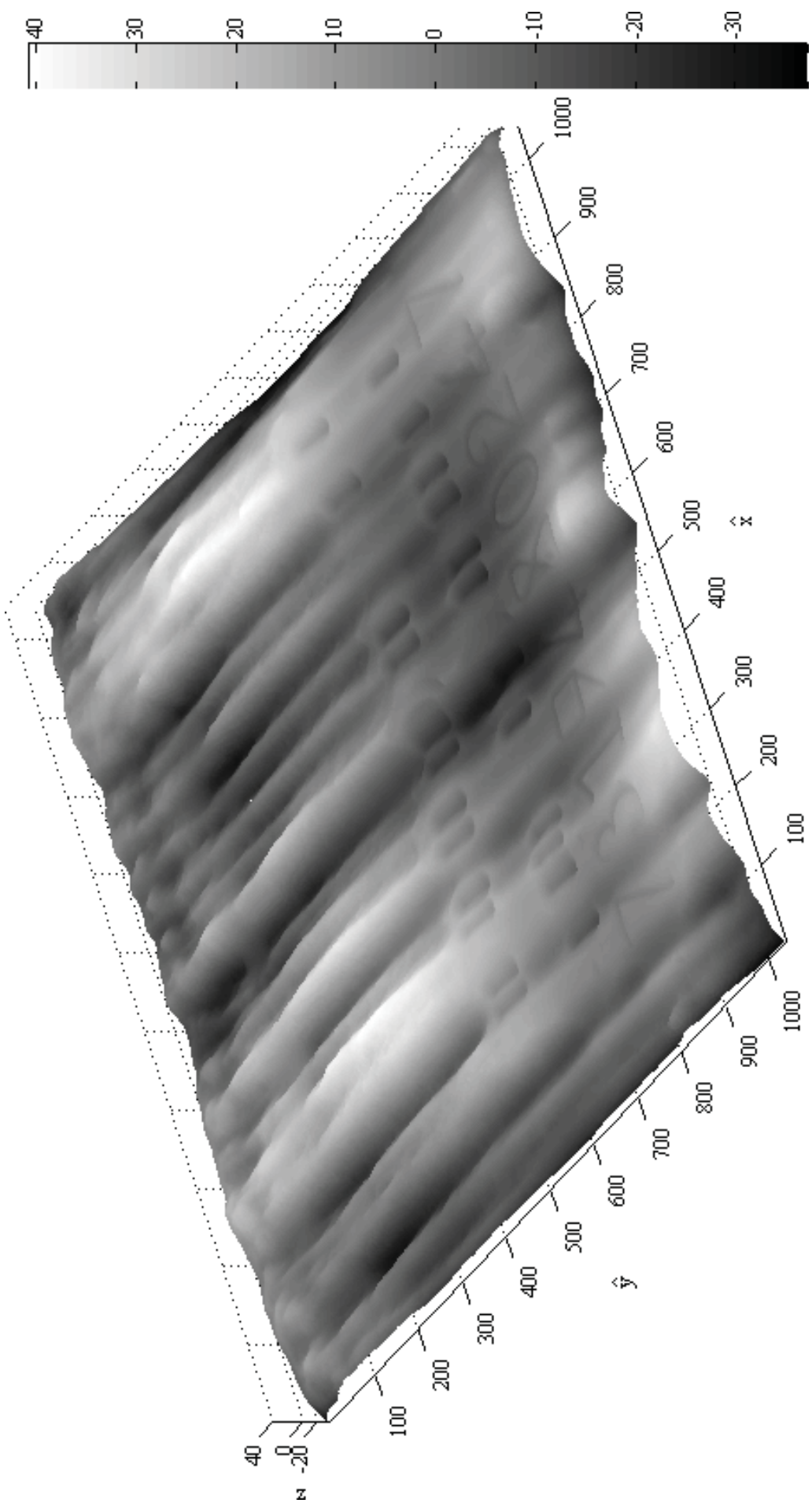

Figure 7.9.: Reconstructed surface after error correction with a two dimensional polynomial surface $\bar{Z}_{\hat{x},\hat{y}} = Z_{\hat{x},\hat{y}} - P_{\hat{x},\hat{y}}$. The grooves in the area covered with scale appear higher than in the label area. The bar code and the numeric code are clearly visible but need to be further separated from the waviness of the surface.

8. Summary and Conclusion

This thesis presented a Photometric Stereo experiment setup. The main sources for errors in the non-ideal setup were identified. It was shown that the light sources used for the different illumination directions for Photometric Stereo varied significantly in terms of the emitted light intensity.

A calibration method was derived to compensate for the inhomogeneous illumination emitted by the light sources. For this purpose, the light distribution of each light source was measured and a calibration matrix was developed. The calibration matrix was used to normalize the source data for the method of Photometric Stereo. However, it was shown that the calibration of the experiment setup does not significantly impact the computational performance of the method.

The error caused by the inhomogeneous illumination increases with the size of the test specimen. The calibration method allows for the surveying of large scale specimens. It was shown that a metallic surface of 17.5x17.5 cm could be reconstructed in a robust manner. A method was presented to compensate the remaining systematic error.

However, several limitations to the method of Photometric Stereo remain; the inhomogeneous light distribution of the illumination and the perspective projection of the camera limit the application of Photometric Stereo, so that only surfaces with small height differences can be measured; furthermore, the Lambertian Reflectance Model limits the method of Photometric Stereo to diffuse surfaces. Surfaces with glossy reflectance behavior cannot be surveyed in a robust manner.

The use of Photometric Stereo in industrial applications is not exclusively limited by the errors induced by the non-ideal test stand. The experiment setup presented in this work operated in a dark room; however, the rough environments in industries, such as steel mills, often prohibit an accurate control of the light conditions. Ambient light and pulsating artificial light falsify the measurements.

In conclusion, the current application for Photometric Stereo is limited to feature and flaw detection of surfaces. The absolute surface height cannot be measured because of the non-ideal surface characteristics, the limit of the method for only diffuse surfaces, and the error caused by the numerical integration for the surface reconstruction. The presented method for calibrating the experiment setup can partially compensate the inhomogeneous illumination emitted by the non-ideal light sources. However, it was shown that despite the calibration, a systematic error in the reconstructed surface still remains.

9. Outlook

The developed calibration method in this paper is progress for the future application of Photometric Stereo in industrial use. However, it cannot correct all systematic errors of the setup. One major error in the setup is caused by the inhomogeneous spatial light distribution and the perspective projection of the camera lens. The method developed in this thesis for calibrating the test stand is an approach to reduce the error induced by these setup imperfections. In order to eliminate the need for the calibration, future improvements to the test stand need to be done:

1. the use of collimated light sources for the scene illumination; and
2. the use of a telecentric camera lens.

A collimated light source applicable for Photometric Stereo needs to have a homogeneous spatial light distribution so that the luminous flux is the same for each position in space. Especially for large scale specimens, the construction of a light source with this property appears to be non-trivial.

A telecentric lens uses orthographic projection to image a specimen on the CCD sensor. This means that if the camera is aligned with the z-axis, a surface patch displaced in the z-direction will always be imaged on the same camera pixel. However, the size of a specimen observed with a telecentric lens is limited to the opening size of the lens.

The most significant limitation of Photometric Stereo is the Lambertian Reflectance Model. This model assumes that the surveyed surface shows ideally diffuse reflectance. The Lambertian model has been used because of its simple implementation and its ideal computational performance. However, in industrial applications, the optical properties of a specimen differ from this idealized assumption and often the properties vary stochastically. Further research needs to focus on a reflectance model applicable to diffuse, glossy and specular reflection. For an inhomogeneous surface, the reflectance behavior of each surface element needs to be determined for a correct application of the reflectance model.

A. Matlab Code

Listing A.1: Calibration of the illumination by calculation of $\rho^*_{\hat{x},\hat{y}}$ and $\bar{\rho}^*_{\hat{x},\hat{y}}$.

```
1  function [rho_star_filtered1,rho_star_filtered2,
       rho_star_filtered3,rho_star_filtered4] =
       illuminationCalibration(I_star1,I_star2,I_star3,I_star4)
2  %lightCalibration Calculates calibration matrices
3  %rho_star_filtered to normalize source images I
4  %for use with Photometric Stereo.
5  %
6  %   I_star1 - I_star4 are images of a diffuse plane
7  %   calibration surface. The light distribution of
8  %   the incident illumination is visible on these
9  %   images.
10 %
11 %   The output rho_star_filtered1 - rho_star_filtered4
12 %   is used to normalize source images I for the use
13 %   with Photometric Stereo by calculating
14 %
15 %               In = I ./ rho_star_filtered .
16 %
17 % Author :  Georg Jaindl
18 % Date :    22 October 2009
19
20 % Casting input images from integer to double.
21 I_star1=double(I_star1);
22 I_star2=double(I_star2);
23 I_star3=double(I_star3);
24 I_star4=double(I_star4);
25
26 % Geometry information of the experiment setup. All units in
       millimeter
27 geometry.hl = 920;
28 geometry.ho = 10;
29 geometry.dl1 = 410;
30 geometry.dl2 = 410;
31 geometry.dl3 = 410;
32 geometry.dl4 = 410;
```

```
33 % Angular position of the light sources measured from the x-
      axis (in radians).
34 geometry.tl1 = (3*pi) / 4 ;
35 geometry.tl2 = (1*pi) / 4 ;
36 geometry.tl3 = (7*pi) / 4 ;
37 geometry.tl4 = (5*pi) / 4 ;
38 % Dimensions of the area observed by the camera.
39 geometry.xmin = -88;
40 geometry.xmax =  88;
41 geometry.ymin = -88;
42 geometry.ymax =  88;
43
44 % Position of each image pixel in global coordinates.
45 global_coordinates = zeros(1040,1040,3);
46 for i = 1 : 1040
47     global_coordinates(i,:,1) = linspace(geometry.xmin,geometry
          .xmax,1040);
48     global_coordinates(:,i,2) = linspace(geometry.ymax,geometry
          .ymin,1040)';
49 end
50
51 % Position of the light sources in global coordinates.
52 position_light1 = [ geometry.dl1 * [ cos(geometry.tl1), sin(
      geometry.tl1) ], geometry.hl-geometry.ho ] ;
53 position_light2 = [ geometry.dl2 * [ cos(geometry.tl2), sin(
      geometry.tl2) ], geometry.hl-geometry.ho ] ;
54 position_light3 = [ geometry.dl3 * [ cos(geometry.tl3), sin(
      geometry.tl3) ], geometry.hl-geometry.ho ] ;
55 position_light4 = [ geometry.dl4 * [ cos(geometry.tl4), sin(
      geometry.tl4) ], geometry.hl-geometry.ho ] ;
56
57 % Vector s pointing from each pixel to the light source.
58 s1(:,:,1) = position_light1(1) - global_coordinates(:,:,1);
59 s1(:,:,2) = position_light1(2) - global_coordinates(:,:,2);
60 s1(:,:,3) = position_light1(3) - global_coordinates(:,:,3);
61
62 s2(:,:,1) = position_light2(1) - global_coordinates(:,:,1);
63 s2(:,:,2) = position_light2(2) - global_coordinates(:,:,2);
64 s2(:,:,3) = position_light2(3) - global_coordinates(:,:,3);
65
66 s3(:,:,1) = position_light3(1) - global_coordinates(:,:,1);
67 s3(:,:,2) = position_light3(2) - global_coordinates(:,:,2);
68 s3(:,:,3) = position_light3(3) - global_coordinates(:,:,3);
69
```

```
70  s4(:,:,1) = position_light4(1) - global_coordinates(:,:,1);
71  s4(:,:,2) = position_light4(2) - global_coordinates(:,:,2);
72  s4(:,:,3) = position_light4(3) - global_coordinates(:,:,3);
73
74  % Surfacenormal n of the plane calibration surface.
75  n = [0;0;1];
76
77  % Reciprocal Cosine of angle of the incident light for each
        pixel.
78  reciprocal_cosine_i1=zeros(1040,1040);
79  reciprocal_cosine_i2=zeros(1040,1040);
80  reciprocal_cosine_i3=zeros(1040,1040);
81  reciprocal_cosine_i4=zeros(1040,1040);
82  for y = 1 : 1040
83     for x = 1 : 1040
84        s1_xy = [s1(y,x,1);s1(y,x,2);s1(y,x,3)];
85        reciprocal_cosine_i1(y,x) = norm(n) * norm(s1_xy) / ( n'
             * s1_xy);
86
87        s2_xy = [s2(y,x,1);s2(y,x,2);s2(y,x,3)];
88        reciprocal_cosine_i2(y,x) = norm(n) * norm(s2_xy) / ( n'
             * s2_xy);
89
90        s3_xy = [s3(y,x,1);s3(y,x,2);s3(y,x,3)];
91        reciprocal_cosine_i3(y,x) = norm(n) * norm(s3_xy) / ( n'
             * s3_xy);
92
93        s4_xy = [s4(y,x,1);s4(y,x,2);s4(y,x,3)];
94        reciprocal_cosine_i4(y,x) = norm(n) * norm(s4_xy) / ( n'
             * s4_xy);
95     end
96     disp(strcat('Progress: ',num2str(100*y/1040),'%'));
97  end
98  clear s1_xy s2_xy s3_xy s4_xy;
99
100 % Unfiltered clibration matrix rho_star.
101 rho_star1 = reciprocal_cosine_i1.*I_star1;
102 rho_star2 = reciprocal_cosine_i2.*I_star2;
103 rho_star3 = reciprocal_cosine_i3.*I_star3;
104 rho_star4 = reciprocal_cosine_i4.*I_star4;
105
106 % Filtering of the calibration matrix by fitting
107 % a polynomial surface of degree 10. The function
108 % fit2DPolySurface was kindly provided by Paul O'Leary
```

```
109 % (O'Leary, P. Harker, M. Discrete polynomial moments
110 % for real-time geometric surface inspection. Journal
111 % of Electronic Imaging, 18, Jan-Mar 2009.)
112 polydegX = 10;
113 polydegY = 10;
114 rho_star_filtered1 = fit2DPolySurface(rho_star1,polydegY,
       polydegX);
115 rho_star_filtered2 = fit2DPolySurface(rho_star2,polydegY,
       polydegX);
116 rho_star_filtered3 = fit2DPolySurface(rho_star3,polydegY,
       polydegX);
117 rho_star_filtered4 = fit2DPolySurface(rho_star4,polydegY,
       polydegX);
118
119 % Export of the calibration matrix.
120 save('rho_star_filtered','rho_star_filtered1','
       rho_star_filtered2','rho_star_filtered3','rho_star_filtered4
       ');
```

Listing A.2: Calculation of $\tilde{\mathsf{N}}^{+}$ for each pixel $(\hat{x}, \hat{y})$ in the image.

```
1  function pinvN = pseudoInverseN
2  %angularCalibration calculates the Moore-Penrose
3  %   pseudoinverse of the Matrix N for each pixel of
4  %   an image. The resulting matrix is of the size
5  %   1040x1040x3x4, so that for each 1040x1040 pixel
6  %   of an image a 3x4 matrix is available. pinvN is
7  %   used in Photometric Stereo to determine the
8  %   gradient field of a specimen's surface.
9  %
10 % Author :  Georg Jaindl
11 % Date :    22 October 2009
12
13 % Geometry information of the experiment setup. All units in
       millimeter.
14 geometry.hl = 920;
15 geometry.ho = 10;
16 geometry.d1 = 410;
17 geometry.d2 = 410;
18 geometry.d3 = 410;
19 geometry.d4 = 410;
20 % Angular position of the light sources measured from the x-
       axis (in radians).
21 geometry.t1 = (3*pi) / 4 ;
22 geometry.t2 = (1*pi) / 4 ;
```

```
23 geometry.t3 = (7*pi) / 4 ;
24 geometry.t4 = (5*pi) / 4 ;
25 % Dimensions of the area observed by the camera.
26 geometry.xmin = -88;
27 geometry.xmax =  88;
28 geometry.ymin = -88;
29 geometry.ymax =  88;
30
31 % Position of each image pixel in global coordinates.
32 global_coordinates = zeros(1040,1040,3);
33 for i = 1 : 1040
34     global_coordinates(i,:,1) = linspace(geometry.xmin,geometry
       .xmax,1040);  % lines, x direction
35     global_coordinates(:,i,2) = linspace(geometry.ymax,geometry
       .ymin,1040)'; % columns, y direction
36 end
37
38
39 % Position of the light sources in global coordinates.
40 position_light1 = [ geometry.d1 * [ cos(geometry.t1), sin(
   geometry.t1) ], geometry.hl-geometry.ho ] ;
41 position_light2 = [ geometry.d2 * [ cos(geometry.t2), sin(
   geometry.t2) ], geometry.hl-geometry.ho ] ;
42 position_light3 = [ geometry.d3 * [ cos(geometry.t3), sin(
   geometry.t3) ], geometry.hl-geometry.ho ] ;
43 position_light4 = [ geometry.d4 * [ cos(geometry.t4), sin(
   geometry.t4) ], geometry.hl-geometry.ho ] ;
44
45 % Vector s pointing from each pixel to the light source.
46 s1(:,:,1) = position_light1(1) - global_coordinates(:,:,1);
47 s1(:,:,2) = position_light1(2) - global_coordinates(:,:,2);
48 s1(:,:,3) = position_light1(3) - global_coordinates(:,:,3);
49
50 s2(:,:,1) = position_light2(1) - global_coordinates(:,:,1);
51 s2(:,:,2) = position_light2(2) - global_coordinates(:,:,2);
52 s2(:,:,3) = position_light2(3) - global_coordinates(:,:,3);
53
54 s3(:,:,1) = position_light3(1) - global_coordinates(:,:,1);
55 s3(:,:,2) = position_light3(2) - global_coordinates(:,:,2);
56 s3(:,:,3) = position_light3(3) - global_coordinates(:,:,3);
57
58 s4(:,:,1) = position_light4(1) - global_coordinates(:,:,1);
59 s4(:,:,2) = position_light4(2) - global_coordinates(:,:,2);
60 s4(:,:,3) = position_light4(3) - global_coordinates(:,:,3);
```

```
61
62 % Calculation of pinvN for each pixel.
63 pinvN = zeros(1040,1040,3,4);
64 for y = 1 : 1040
65    for x = 1 : 1040
66        % Normalizing the vector s.
67        s1(y,x,:) = s1(y,x,:) / norm([s1(y,x,1),s1(y,x,2),s1(y,x
             ,3)]);
68        s2(y,x,:) = s2(y,x,:) / norm([s2(y,x,1),s2(y,x,2),s2(y,x
             ,3)]);
69        s3(y,x,:) = s3(y,x,:) / norm([s3(y,x,1),s3(y,x,2),s3(y,x
             ,3)]);
70        s4(y,x,:) = s4(y,x,:) / norm([s4(y,x,1),s4(y,x,2),s4(y,x
             ,3)]);
71
72        N = [ s1(y,x,1), s1(y,x,2), s1(y,x,3)
73              s2(y,x,1), s2(y,x,2), s2(y,x,3)
74              s3(y,x,1), s3(y,x,2), s3(y,x,3)
75              s4(y,x,1), s4(y,x,2), s4(y,x,3) ] ;
76
77        pinvN(y,x,:,:) = pinv(N);
78    end
79    disp(strcat('Progress:', num2str(100*y/1040),'%'));
80 end
81
82 %Export pinvN
83 save('pinvN','pinvN');
```

Listing A.3: Calculation of the gradient field (p, q).

```
1  function [p,q,rho_n] = gradientField(I1,I2,I3,I4)
2  %gradient Calculates the gradient field (p,q) and
3  %   the normalized reflectance factor
4  %   rho_n of a surface from the source images I1 - I4.
5  %
6  % Author :  Georg Jaindl
7  % Date :    22 October 2009
8
9  % Casting input images from integer to double.
10 I1 = double(I1);
11 I2 = double(I2);
12 I3 = double(I3);
13 I4 = double(I4);
14
15 % Normalizing source images.
```

```
16 load('rho_star_filtered');
17 In1 = imdivide( I1, rho_star_filtered1 );
18 In2 = imdivide( I2, rho_star_filtered2 );
19 In3 = imdivide( I3, rho_star_filtered3 );
20 In4 = imdivide( I4, rho_star_filtered4 );
21 clear rho_star_filtered1 rho_star_filtered2 rho_star_filtered3
      rho_star_filtered4;
22 clear I1 I2 I3 I4;
23
24 % Calculating the surface normal vector field.
25 load('pinvN');
26 nx = pinvN(:,:,1,1).*In1 + pinvN(:,:,1,2).*In2 + pinvN(:,:,1,3)
      .*In3 + pinvN(:,:,1,4).*In4 ;
27 ny = pinvN(:,:,2,1).*In1 + pinvN(:,:,2,2).*In2 + pinvN(:,:,2,3)
      .*In3 + pinvN(:,:,2,4).*In4 ;
28 nz = pinvN(:,:,3,1).*In1 + pinvN(:,:,3,2).*In2 + pinvN(:,:,3,3)
      .*In3 + pinvN(:,:,3,4).*In4 ;
29 clear pinvN;
30 clear In1 In2 In3 In4;
31
32 % Calculating the normalized surface reflectance factor.
33 rho_n = sqrt(nx.^2+ny.^2+nz.^2);
34
35 % Calculating the surface gradient field.
36 p = -nx./nz ;
37 q = -ny./nz ;
```

List of Figures

List of Tables

Listings

Bibliography

[1] Harker, M., O'Leary, P. Least squares surface reconstruction from measured gradient fields. Technical report, University of Leoben, Institute for Automation, 2008.

[2] Horn, B. K. P., Sjober, R. W. Calculating the reflectance map. *Applied Optics*, 18(11):1770–1779, June 1979.

[3] JAI. *AccuPiXEL^{TM} LUT (Look-Up Table) Function*, July 2000. TH-1086.

[4] JAI. *Camera Sensitivity Explained*, May 2007. TN-0701.

[5] JAI. *Using a 2CCD Camera to Create High-Dynamic Range Images*, February 2009. TN-0902.

[6] JAI PULNiX. *Pulnix TM-1400 Datasheet*.

[7] North Coleman, E. Jr., Jain, R. *Shape recovery*, chapter Obtaining 3-dimensional shape of textured and specular surfaces using four-source photometry, pages 180–199. Jones and Bartlett Publishers, Inc., 1992.

[8] Ohenhen, G. Photometric stereo applied to metallic surface inspection. Master's thesis, University of Leoben, Austria, December 2007.

[9] O'Leary, P. Harker, M. Discrete polynomial moments for real-time geometric surface inspection. *Journal of Electronic Imaging*, 18, Jan-Mar 2009.

[10] Osram GmbH. *DRAGONeye Data Sheet*, January 2009.

[11] Woodham, R. J. Photometric method for determining surface orientation from multiple images. *Optical Engineering*, 19(1):139–144, January/February 1979.